Programmable Synthesis of Multimetallic Phosphide Nanorods Mediated by Core/Shell Structure Formation and Conversion

Yulu Zhang,^{†, #} Na Li,^{‡, #} Zhiyong Zhang,[†] Shuang Li,[‡] Meiyang Cui,[†] Lu Ma,[§] Hua Zhou,[△] Dong Su,^{‡, ⊥} Sen Zhang^{*, †}

- † Department of Chemistry, University of Virginia, Charlottesville, Virginia 22904, United States;
- [‡] Center for Functional Nanomaterials, Brookhaven National Laboratory, Upton, New York 11973, United States;
- § National Synchrotron Light Source II, Brookhaven National Laboratory, Upton, New York 11973, United States;
- ^Δ X-ray Science Division, Advanced Photon Source, Argonne National Laboratory, Lemont, Illinois 60439, United States;
- ¹ Present address: Beijing National Laboratory for Condensed Matter Physics, Chinese Academy of Sciences, Beijing 100190, China.

ABSTRACT: Generalized synthetic strategies for nanostructures with well-defined physical dimensions and broad-range chemical compositions are at the frontier of advanced nanomaterials design, functionalization, and application. Here, we report a composition-programmable synthesis of multimetallic phosphide $CoMP_x$ nanorods (NRs) wherein M can be controlled to be Fe, Ni, Mn, Cu, and their binary combinations. Forming Co_2P/MP_x core/shell NRs and subsequently converting them into $CoMP_x$ solid-solution NRs through thermal post-treatment are essential to overcome the obstacle of morphology/structure inconsistency faced in conventional synthesis of $CoMP_x$ with the different M compositions. The resultant $CoMP_x$ with uniform 1-dimensional (1-D) structure provides us a platform to unambiguously screen the M synergistic effects in improving the electrocatalytic activity, as exemplified by the oxygen evolution reaction (OER). This new approach mediated by core/shell nanostructure formation and conversion can be extended to other multi-component nanocrystal systems (metal alloy, mixed oxide and chalcogenide, *etc.*) for diverse applications.

1. INTRODUCTION

Metal phosphide nanostructures have attracted much attention during the past decades due to their unique magnetic, semiconducting, mechanical, and catalytic properties. 1-4 Compared with zero-dimensional (0-D) nanoparticles, 1-D metal phosphide nanorods (NRs)/nanowires (NWs) are of particular interests, as the strong anisotropic effect presents new opportunity to tune their physicochemical properties and functionalization potentials.⁵⁻⁸ Among a variety of synthetic approaches, organic phase colloidal synthesis has been proven effective in generating size/structure-uniform metal phosphide nanocrystals, through either the direct decomposition of metal-phosphine organometallic complexes or the indirect process of phosphidation transforming pre-made metal/metal oxide to metal phosphide. 9-15 Both routes, especially the former one, are well established for mono-metallic phosphide NRs/NWs, including Ni₂P, Fe₂P, Co₂P, MnP, etc. 16-20 However, it is still rare to produce multimetallic phosphide NRs/NWs, because of the variation in the decomposition temperatures and rates of different metal-phosphine complexes and the complex solid growth kinetics of multimetallic phosphides, making it challenging to form 1-D NRs/NWs rather than 0-D nanoparticles. 11-12, 21

In this article, we report a strategy for the synthesis of multimetallic phosphide CoMP_x NRs with M programmable among Fe, Ni, Mn, Cu, and their binary combinations. Our previous study demonstrated that monodisperse Co₂P NRs can be synthesized and used as seeds to produce Co₂P/Pt core/shell NRs without changing 1-D shape uniformity. 18, 22 With this success, we anticipate that such a seed-mediated synthesis can also lead to the formation of Co₂P/MP_x while preserving with the same level of 1-D structural control. Our experiment confirmed this hypothesis, as illustrated in Fig. 1, leading to a group of Co₂P/MP_x core/shell NRs with tunable M compositions and Co/M ratios. Interestingly, the Co₂P/MP_x NRs can be converted into CoMP_x NRs with solid-solution structure, after being loaded onto a support (e.g. carbon, Al₂O₃, or TiO₂) and a subsequent interfacial diffusion, promoted by thermal treatment. In contrast, the direct synthesis of CoMP_x by co-decomposing Co- and M-phosphine complexes yielded products with uncontrollable shapes/structures (Fig. 1). The 1-D shape/structure consistency and programmable composition presented by the CoMP_x NRs herein make it possible to refine the composition-property relationship, especially for catalysis, while excluding the impact of size/shape/structural parameters. Using the oxygen evolution reaction (OER) as a model reaction, we demonstrated that the modulation of M composition can substantially tune the catalytic performance of CoMP_x NRs.

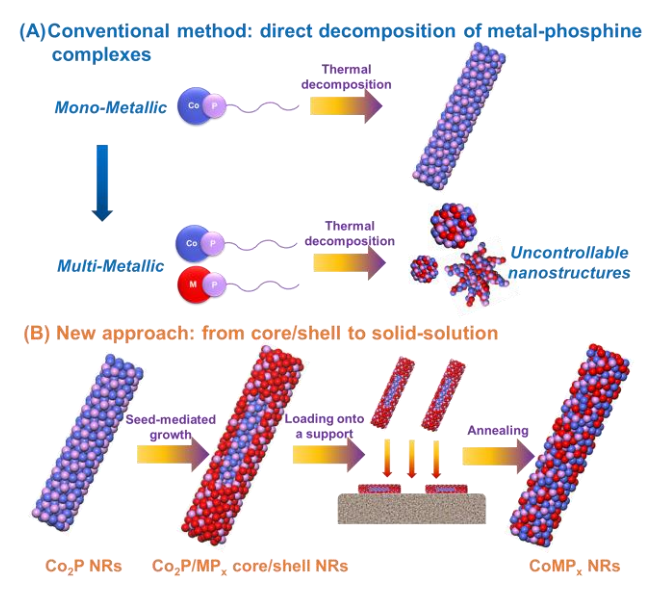


Figure 1. Schematic illustration of conventional synthetic method and our new approach to multimetallic phosphide 1-D NRs/NWs. (A) Conventional synthesis via direct decomposition of metalphosphine complexes, which is prone to the formation of uncontrolled nanostructures with irregular morphologies when using multimetallic phosphine complexes. (B) New approach to CoMP_x NRs mediated by core/shell nanostructure formation in this work.

2. EXPERIMENTAL SECTION

2.1 Materials. Cobalt acetate tetrahydrate (Co(ac)₂•4H₂O, >98%), benzyl ether (BE, 98%), oleic acid (OAc, 90%), tributylphosphine (TBP, 97%), Nafion (5 wt% in lower aliphatic alcohols and water) and Titanium (IV) oxide nanopowder (21 nm, P25) were purchased from Sigma-Aldrich. 1-octadecene (ODE, 90%), copper acetylacetonate (Cu(acac)₂, 98%) and nickel acetylacetonate (Ni(acac)₂, 96%) were purchased from Acros Organics. Iron acetylacetonate (Fe(acac)₃, 99%) and manganese acetylacetonate (Mn(acac)₂, 95%) were purchased from Strem Chemicals. Isopropanol (99.5%) and hexanes (98.5%) were purchased from Fisher Scientific. Multi-walled carbon nanotubes (8 nm in diameter) were purchased from CheapTubes. Vulcan-72 carbon black was obtained from Fuel Cell Store. Aluminum oxide (13nm, 99.8%) was purchased from Alfa Aesar. All chemicals and materials were used without further purification.

2.2 Synthesis of Co₂P NRs. All wet-chemical syntheses were performed using standard Schlenk techniques. 2 g of Co(ac)₂•4H₂O was mixed with 80 ml of BE (or ODE) and 8 ml of OAc. The mixture was magnetically stirred and heated to 140°C under the flow of N₂. After the full dissolution of Co(ac)₂•4H₂O, the mixture was cooled to 100°C and kept under vacuum for 1 hour to remove moisture and impurities. The system was then filled with N₂ and heated to 220°C at a rate of ~ 5°C min⁻¹. Subsequently, 12 ml of TBP was injected into the solution and the mixture was aged at 260°C (in reflux) for 2 hours. After cooling down to the room tempera-

ture, the NRs were separated by adding isopropanol followed by centrifugation (8000 rpm, 8 min). The NRs were further purified by 2-3 cycles of dispersion (using hexane) and precipitation (by adding isopropanol). The Co₂P NRs were re-dispersed and stored in hexanes for further use. This synthesis produces Co₂P NRs with an average length of 24.7 nm. Using ODE as a solvent and performing reaction at 280°C yield Co₂P NRs with an average length of 36.5 nm.

2.3 Synthesis of Co₂P/MP_x core/shell NRs. In a typical synthesis of Co₂P/NiP_x core/shell NRs, a certain amount of Ni(acac)₂ was dissolved in the mixture of 10 ml of BE and 0.2 ml of OAc at 100°C under vacuum for 1 hour. Under N₂, a hexane solution containing Co₂P seeds was injected into the reaction solution. The system was then briefly vacuumed for 5 minutes to remove hexane, and refilled with N2. Subsequently, 0.3 ml of TBP was injected into the system and the mixture was heated to 260°C at a rate of 2°C min⁻¹ and maintained at that temperature for 1 hour. The Co₂P/NiP_x core/shell NRs were collected and purified using the same procedure for Co₂P NRs. Using Fe(acac)₃, Mn(acac)₂ or Cu(acac)₂ precursors, or their binary combinations, the Co₂P/MP_x core/shell NRs with different M compositions were synthesized. The as-prepared Co₂P/MP_x NRs were stored in hexane. By tuning the amount of Co₂P seed and metal precursor, the Co/M ratio in the as-obtained core/shell NRs was readily designed and adjusted, as summarized in Table S1.

2.4 Converting Co₂P/MP_x core/shell NRs to CoMP_x solid-solution NRs. In a typical process with carbon nanotube (CNT), an equal weight of Co₂P/MP_x NRs and CNT were sonicated together in 30 ml of hexane for 1 hour. The CNT-supported NRs (CNT-Co₂P/MP_x) were then collected by centrifugation, dried under vacuum, and annealed under forming gas (5% H₂ in N₂) at 400°C for 2 hours to generate CNTs-supported solid-solution CoMP_x NRs (CNT-CoMP_x). Other supports, such as Vulcan-72 carbon black, Al₂O₃, and TiO₂, can be used in the same manner, and the corresponding supported NRs are denoted as C-, Al₂O₃-, and TiO₂-Co₂P/MP_x or CoMP_x, respectively. The CNT was specifically used as a supporting material for electrocatalysis in our studies.

2.5 Material Characterizations. Quantitative elemental analyses for the composition of NRs were carried out with inductively coupled plasma optical emission spectrometry (ICP-OES) on a Perkin Elmer Avio-200 ICP spectrometer. Transmission electron microscopy (TEM) images were obtained using a FEI Tecnai Spirit (120 kV). Scanning transmission electron microscopy (STEM) analyses were carried out using a Hitachi HD2700C (200 kV) with a probe aberration-corrector, in the Center for Functional Nanomaterials at Brookhaven National Laboratory. The electron energy-loss spectroscopy (EELS) mappings were collected using a high resolution Gatan-Enfina ER with a probe size of 1.3Å. A power law function was used for EELS background subtraction. X-ray photoelectron spectroscopy (XPS) was carried out on a Phi X-tool instrument with Mg K α (h ν =1253.6 eV) as the excitation source. The binding energies obtained in the XPS spectral analysis were corrected for specimen charging by referencing C 1s to 284.8 eV. The synchrotron radiation X-ray diffraction (SR-XRD) was performed at 7BM QAS beamline at National Synchrotron Light Source II (NSLS-II), Brookhaven National Laboratory. The X-ray was monochromated with silicon 111 crystal to 20 keV. The diffraction pattern was collected in a transmission way with a PerkinElmer 1621 area detector about 294 mm away from the sample. LaB $_6$ powder was used to calibrate the distance and the tilting of the detector. The diffraction patterns were integrated and analyzed by the DIOPTAS software.

2.6 Electrochemical Characterizations. The electrochemical analyses were performed on a Biologics VMP3 potentiostat in a three-electrode system consisting of a glassy carbon rotating disk electrode (RDE, 5 mm in diameter), a Hg/HgO reference electrode (1.0 M KOH), and a platinum foil counter electrode. The Hg/HgO (1.0 M KOH) electrode was calibrated vs. reversible hydrogen electrode (RHE) prior to electrochemistry to allow all potentials to be reported vs. RHE in this work. To prepare a working electrode, 5 mg of CNT-supported catalyst was dispersed in a mixture of water. isopropanol and Nafion (500 µl, 500 µl and 5 µl, respectively) by sonication to form a catalyst ink. An appropriate amount of the ink was then dropcast onto the surface of RDE, forming a uniform catalyst layer with a metal mass loading of 10 µg. The OER performances of catalysts were then investigated in an O₂-saturated 1.0 M KOH via a linear polarization from 0.926 to 1.726 V vs. RHE at 10 mV s⁻¹ and 1600 rpm. We also evaluated the OER activity of these catalysts using a Ni foam electrode, on which the as-prepared catalyst ink was dropcast with a mass loading of 1 g_{metal} cm⁻ ². The electrode was sealed with epoxy with an exposed area of 1 cm². Then the stabilities of these catalysts were assessed by chronopotentiometry at a constant current density of 20 mA cm⁻² for 10 hours, followed by at 50 mA cm⁻² for another 10 hours in an O₂-saturated 1.0 M KOH electrolyte.

3. RESULTS AND DISCUSSION

The synthesis of multimetallic phosphide NRs/NWs, using $CoNiP_x$ as an example, was first studied via the direct co-decomposition of Co- and Ni-TBP complexes in a one-pot reaction. This procedure is derived from our previous synthesis of Co_2P NRs (Experimental section).¹⁸ We found that the addition of Ni precursor, even in a small amount (Co:Ni molar ratio in reactants = 19:1 or 14:1), led to the formation of 0-D nanoparticles (**Fig. S1**). The nanoparticles become the primary product when increasing the Ni content. For example, at the molar ratio of Co:Ni = 1:1, monodisperse nanoparticles with a diameter of 3 nm were obtained. Other irregular morphologies were observed when replacing Ni with different M (M = Fe, Mn, Cu) precursors (**Fig. S2**), indicating that this one-step process is insufficient to prepare well-defined multimetallic phosphide NRs/NWs.

The new approach highlighted in **Fig. 1B** takes advantage of the templating effect of pre-made Co_2P NRs to achieve the dimension control via the seed-mediated growth (Experimental section). In the first step of synthesizing Co_2P NR seeds, using different synthesis temperatures, we obtained Co_2P NRs with a constant width of 3.2 ± 0.9 nm and a tuna-

ble length of 24.7 \pm 3.7 nm and 36.5 \pm 7.2 nm at 260°C (reaction in BE or ODE) and 280°C (reaction in ODE), respectively, as shown in the TEM images in Fig. 2A and S3. The Co₂P/MP_x core/shell NRs were then produced by the decomposition of M-TBP complex in the presence of Co₂P seeds. We found that the Co₂P NRs efficiently serve as a template to guide the uniform coating of MP_x. Fig. 2B-C and S4 show the representative TEM images of Co₂P/NiP_x, Co₂P/MnP_x and Co₂P/FeP_x, confirming that these Co₂P/MP_x NRs well retained the 1-D shape of seeds. Moreover, the M concentration within Co₂P/MP_x NRs can be simply tuned by adjusting the molar ratio of Co₂P seeds and M precursors. As clearly seen in the TEM images in Fig. 2D-F and S5, similar NRs were obtained with Co:M atomic ratio tunable in a wide range from $\sim 3:1$ to $\sim 1:1$, as examined with ICP-OES (**Table** S1). In addition, the sizes of Co₂P/MP_x are also controllable by using Co₂P seeds with different lengths (Fig. S4-S5).

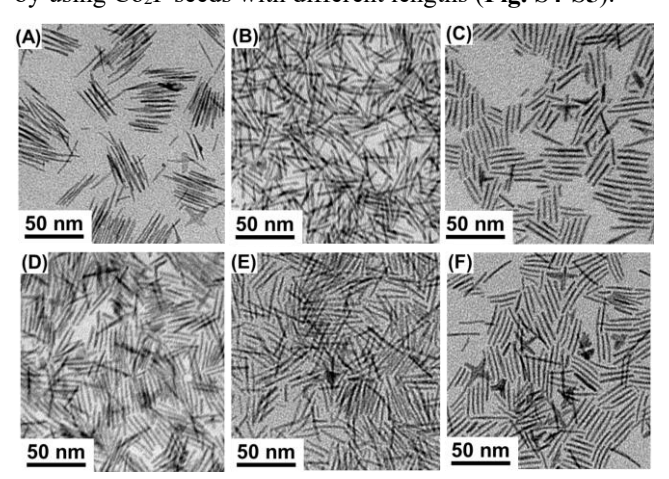


Figure 2. (A) TEM image of Co₂P NRs with an average length of 36.5 nm. (B, C) TEM images of as-synthesized Co₂P/MP_x NRs with MP_x being NiP_x (B) and MnP_x (C); The Co:M atomic ratios are \sim 2:1 in these NRs. (D-F) TEM images of Co₂P/FeP_x NRs with Co:Fe ratio of \sim 3:1 (D), \sim 2:1 (E) and \sim 1:1(F) in these NRs. All syntheses were carried out using 36.5 nm Co₂P seeds.

The STEM high-angle angular dark-field (HAADF) images of as-synthesized Co₂P/MP_x NRs in Fig. S6 and S7 demonstrate that the uniform core/shell structures are generated, with a crystalline core surrounded by an amorphous shell for all observed NRs. The core/shell architectures are further characterized by the STEM electron energy loss spectroscopy (EELS) 2-D elemental mapping, as shown in Fig. 3. For Co₂P/NiP_x, it is clearly seen that Co is concentrated in the core region, which is encapsulated by a Ni shell (Fig. 3D, G, J). Such a core/shell structure is also confirmed with a high-resolution EELS 1-D line scan across an individual Co₂P/NiP_x NR (**Fig. 4A, B**), which presents a typical Co-core and Ni-shell distribution. Similar results are also observed on other Co₂P/MP_x NRs in both 2-D elemental mappings (Fig. 3E, F, H, I, K, L) and 1-D line scans (Fig. S8). Interestingly, these MP_x shells are amorphous regardless of M compositions, even after a reaction at high temperature (280℃). It is probably due to the crystal lattice mismatch between Co₂P and MP_x, which favors the formation of amorphous shell, rather than crystalline one, to minimize core/shell interfacial energy. This substrate-induced crystal structure change was also reported in previous studies of metal/metal and metal sulfide/metal core/shell nanomaterials.²³⁻²⁵

This seed-mediated growth was further extended to make more complex $\text{Co}_2\text{P/MP}_x$ NRs. For example, trimetallic phosphide $\text{Co}_2\text{P/FeNiP}_x$ and $\text{Co}_2\text{P/MnNiP}_x$ NRs were produced using the corresponding mixed M precursors in the reaction (**Fig. S9**). As demonstrated in **Fig. S10**, a shell consisting of both Fe and Ni was observed in STEM EELS 2-D elemental mapping. It suggests that this approach is a generalized synthetic strategy for $\text{Co}_2\text{P/MP}_x$ core/shell NRs with unprecedented tunability in M composition.

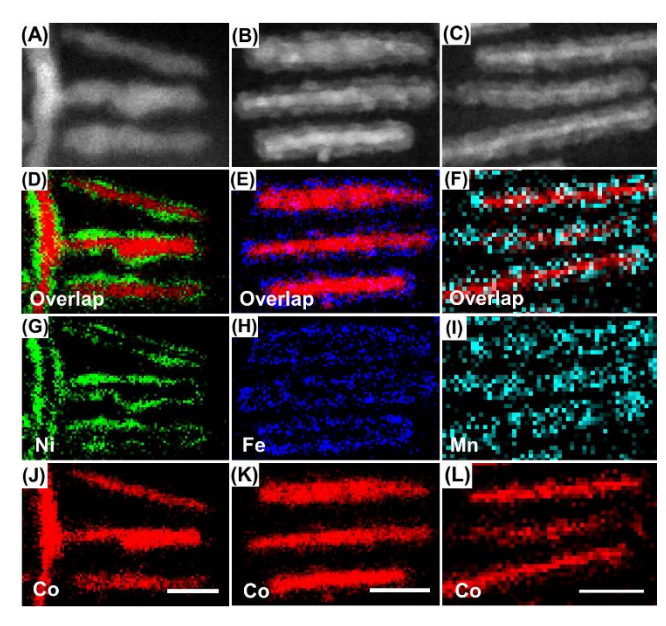


Figure 3. (A-C) STEM-HAADF images and (**D-L**) EELS 2-D elemental mappings of Co₂P/NiP_x (A, D, G, J), Co₂P/FeP_x (B, E, H, K), and Co₂P/MnP_x (C, F, I, L) NRs. These Co₂P/MP_x core/shell NRs have Co:M atomic ratios of ~2:1. Scale bars are 10 nm. All syntheses were carried out using 24.7 nm Co₂P seeds.

Based on the programmable synthesis of core/shell NRs, we found that they can be easily converted into solid-solution CoMP_x NRs via thermal annealing in a reductive gas environment. Prior to this conversion, the Co₂P/MP_x NRs were loaded onto a supporting material to prevent the aggregation of NRs at high temperatures. The reductive gas environment (forming gas, 5% H₂ balanced in N₂) was used to minimize the oxidation of NRs. With a CNT support and an annealing treatment at 400 °C, the resultant NRs exhibited well-preserved size and shape and typical solid-solution structure. These characteristics are observed in their STEM HAADF images (Fig. S11) and 2-D elemental mapping (Fig. 4E-H), where Co and Ni elements are uniformly distributed in a treated CNT-Co_{1.30}Ni_{0.70}P_x NR (Co:Ni ratio is ~2:1). High resolution 1-D line scan on a treated Co_{1.30}Ni_{0.70}P_x NR also reveals a clear transition from core/shell to solid-solution structure through atom diffusion in this process (Fig. 4A-D).

Furthermore, this strategy can be used with different supporting materials, including carbon black (Vulcan-72), Al₂O₃, and TiO₂ (P25), as evidenced by the consistent NR

size and shape of samples after thermal treatments (Fig. S12). It is worth noting that the wide adaptability of this method with various supporting materials is important for the application of $CoMP_x$ in different areas. For example, CNT- and C-CoMP_x NRs can be used for electrocatalysis due to the excellent electrical conductivity of carbon supports. $^{26\text{-}27}$ Al₂O₃ and TiO₂ are widely used in supporting thermal catalysts while providing distinct surface properties, such as surface oxygen reactivity, surface adsorbate profile, and acidity/basicity. $^{28\text{-}30}$ Our CoMP_x NRs supported on different metal oxides is likely to open up new opportunities for modulating heterogeneous catalytic properties.

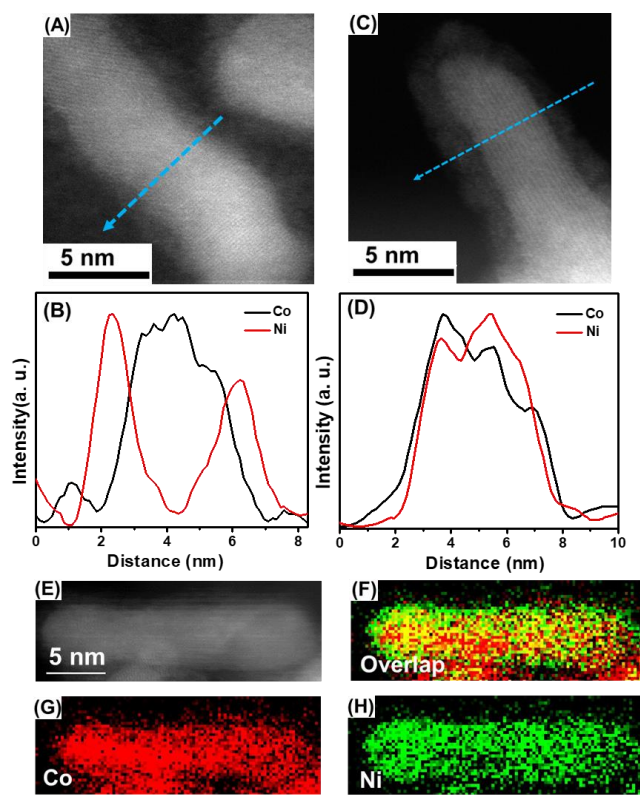


Figure 4. (A, B) STEM-HAADF image and 1-D line scan crossing a Co_2P/NiP_x NR (Co:Ni ratio is \sim 2:1). (C, D) STEM-HAADF image and 1-D line scan crossing a $Co_{1.30}Nio_{.70}P_x$ NR (Co:Ni ratio is \sim 2:1) after treatment in forming gas at 400°C for 2 hours. (E-H) STEM-EELS elemental mapping for $Co_{1.30}Nio_{.70}P_x$. Both samples were supported on CNT, and the synthesis was carried out using 24.7 nm Co_2P seeds.

The crystal structure of Co₂P/MP_x core/shell, bimetallic CoMP_x, and trimetallic CoM₁M₂P_x NRs were investigated using SR-XRD analysis (**Fig. 5A**). Previous studies on metal phosphide NCs, including our study on Co₂P NRs, revealed that metal phosphide is subject to surface oxidation and can easily form an amorphous oxide shell on the surface.³¹⁻³² This amorphous shell can result in an attenuated signal and weak diffraction intensity in lab-XRD analysis.³³ Similarly, our solid-solution CoMP_x NRs produced by thermal annealing also have an amorphous layer in the surface due to the oxidation (**Fig. 4C** and **S11**), and cannot be precisely characterized by lab-XRD. Compared with the lab X-ray sources, high brilliance and high energy synchrotron X-ray photons enable rapid and accurate evaluations of crystal structure.³⁴

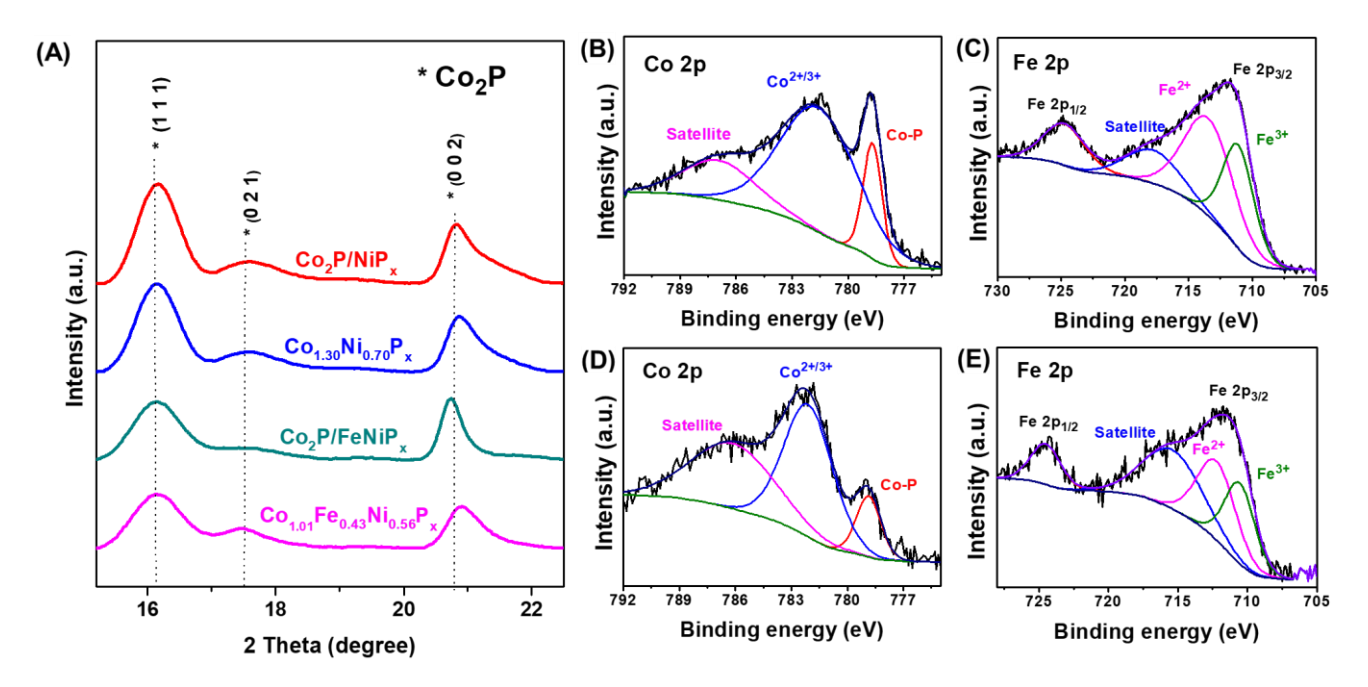


Figure 5. (A) SR-XRD patterns of C-Co₂P/NiP_x (Co:Ni ratio is ~2:1) and C-Co₂P/NiFeP_x (Co:Fe:Ni ratio is ~2:1:1) NRs and their annealed samples (C-Co_{1.30}Ni_{0.70}P_x and C-Co_{1.01}Ni_{0.43}Fe_{0.56}P_x). (B-E) High resolution XPS spectra of C-Co₂P/FeP_x (Co:Fe ratio is ~2:1) before (B, C) and after annealing (D, E). All syntheses were carried out using 36.5 nm Co₂P seeds.

Therefore, the Co₂P/MP_x core/shell and solid-solution CoMP_x NRs are carefully characterized with SR-XRD here, instead of lab-XRD, to obtain increased diffraction intensity and signal-to-noise quality. For pristine Co₂P NRs supported on C (Fig. S13), we observed a typical orthorhombic-phase Co₂P pattern (JCPDS 00-054-0413), with the peaks at 16.1° and 20.7° indexed to Co₂P (111) and (002) lattices, respectively. The peak at 17.7° was also seen, corresponding to an overlap of Co₂P (021) and carbon background. After the seed-mediated growth to core/shell NRs, these Co₂P characteristic peaks are presented without major changes in the C-Co₂P/NiP_x and Co₂P/FeNiP_x core/shell NRs since the synthesized MP_x shells are amorphous (Fig. 5A). Interestingly, the conversion to C-CoMP_x NRs causes negligible change in SR-XRD pattern shape but a slight peak shift. It suggests that the incorporation of M only has an impact on lattice distance and the resultant CoMPx NRs possess a high structural robustness in crystal phase (orthorhombic).

We also performed XPS analysis to understand the surface chemical features of Co₂P, Co₂P/MP_x, and CoMP_x NRs (**Fig. S14** and **S15**). **Fig. S15** shows high resolution Co 2p_{3/2} spectrum of the C-Co₂P NRs. The peak at 778.7 eV is assigned to the binding energy of Co 2p_{3/2} in the Co₂P, while another peak at 781.9 eV is related to Co²⁺ or Co³⁺ in the CoO_x that is generated from the surface oxidation. On the C-Co₂P/FeP_x core/shell NRs, three additional peaks are observed in the Fe 2p_{3/2} region (**Fig. 5C**), corresponding to Fe³⁺ (711.2 eV), Fe²⁺ (713.8 eV), and the satellite peak (717.9 eV).^{9, 35-37} However, we observed no shift in Co 2p_{3/2} peak positions (**Fig. 5B**), indicating that negligible or very weak electron transfer occurs between the crystalline Co₂P core and the amorphous FeP_x shell. After the annealing treatment,

the as-obtained C-Co_{1.33}Fe_{0.67}P_x NRs show a downshift on both Fe³⁺ (710.7 eV) and Fe²⁺ (712.6 eV) peaks (**Fig. 5E**), as well as a slight upshift in Co-P (778.9 eV) and Co^{2+/3+} (782.2 eV) peaks (**Fig. 5D**), implying an electron transfer from Co to Fe in the solid-solution NRs. Similar peak shifts of Co-P and Co^{2+/3+} are also observed in bimetallic C-Co_{1.10}Fe_{0.90}P_x (**Fig. S16**), C-Co_{1.25}Cu_{0.75}P_x (**Fig. S17**), C-Co_{1.25}Mn_{0.75}P_x (**Fig. S18**), C-Co_{1.25}Cu_{0.75}P_x (**Fig. S19**), as well as trimetallic C-Co_{1.01}Fe_{0.43}Ni_{0.56}P_x (**Fig. S20**), indicating that the strong coupling between Co to M associated with solid-solution structure is universal in our CoMP_x NRs.

As an important class of catalytic materials, metal phosphides hold great potential in many thermal catalytic (e.g. hydrogenation, hydrodesulfurization and hydrodenitrogenation reactions) and electrocatalytic (e.g. hydrogen evolution reaction (HER), oxygen reduction reaction (ORR) and oxygen evolution reaction (OER)) reactions.^{9, 38-40} Many previous studies point out that bimetallic materials exhibit more excellent catalytic activities than the monometallic ones, especially for the OER. 21, 41-42 However, an accurate search for optimal bimetallic or multimetallic phosphide candidates for a specific catalytic reaction has been obstructed by the lack of synthetic strategy that can isolate the composition effect from others variables (size, shape, crystal phase etc.). Using the OER as a model reaction, we demonstrate that the programmable synthesis of CoMP_x NRs with highly consistent 1-D morphology and structure can provide an unprecedented opportunity to rapidly screen the multicomponent composition effect.

The bimetallic CNT-CoMP_x NRs were systematically studied in the electrochemical system described in the Experimental Section. Fig. 6A shows the linear polarization curves of CNT-Co₂P and -CoMP_x NRs under the same conditions. The pristine CNT-Co₂P NRs require an OER overpotential (η) of 372.2 mV to achieve a current density (j) of 10 mA cm_{geo}-2 (geo indicates current density normalized over electrode geometric area). In the control experiments without Co₂P or CoMP_x NRs, negligible current is seen on the CNT and RDE in the investigated potential range (Fig. **S21**). The OER activity is largely improved on the bimetallic CNT-CoMP_x NRs and is tunable by altering M compositions (Fig. 6A, B). Keeping the NR composition constant with Co:M ratio of ~2:1, we found that the highest OER activity is achieved on the CNT-Co_{1.33}Fe_{0.67}P_x (η =293.4 mV), which is superior to the CNT-Co_{1.30}Ni_{0.70}P_x (η =338.2 mV), CNT- $Co_{1.25}Mn_{0.75}P_x$ ($\eta = 362.5$ mV) and CNT- $Co_{1.25}Cu_{0.75}P_x$ (η =369.0 mV) NRs catalysts at 10 mA cm_{geo}-2 (Fig. 6B). Clearly, Fe is a more suitable component than others to be coupled with Co to improve the OER kinetics. It can be further evidenced by the lower Tafel slope of CNT-Co_{1.33}Fe_{0.67}P_x (42.5 mV dec⁻¹), compared with other bimetallic catalysts when Co:M ratio is $\sim 2:1$ (Fig. S22).

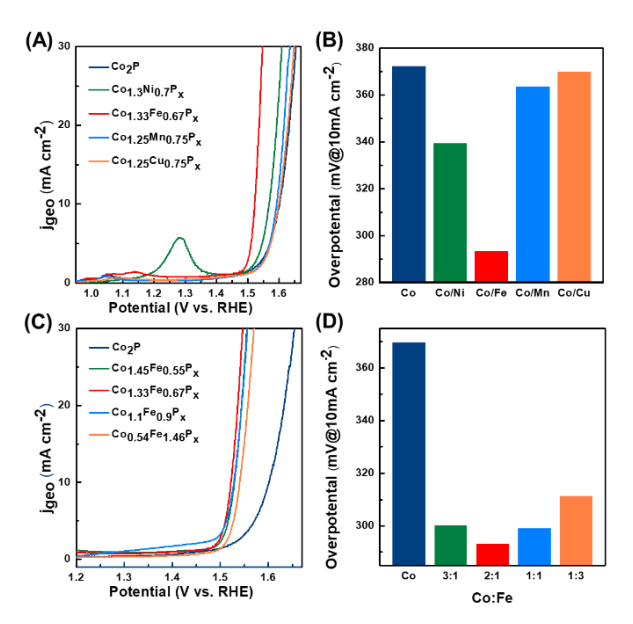


Figure 6. (A, B) OER polarization curves (A) of CNT-Co₂P, -Co_{1.30}Ni_{0.70}P_x, -Co_{1.33}Fe_{0.67}P_x, -Co_{1.25}Mn_{0.75}P_x and -Co_{1.25}Cu_{0.75}P NRs and the comparison of their overpotentials at current density of 10 mA cm_{geo}⁻² (B). (C, D) OER polarization curves (C) of CNT-Co₂P, -Co_{1.45}Fe_{0.55}P_x, -Co_{1.33}Fe_{0.67}P_x, -Co_{1.10}Fe_{0.90}P_x and -Co_{0.54}Fe_{1.46}P_x NRs and the comparison of their overpotentials at current density of 10 mA cm_{geo}⁻² (D). All electrochemical tests were performed in 1.0 M KOH.

The enhancement from Fe incorporation was further optimized by controlling Fe content. As described in **Fig. 6C** and **6D**, a volcano-like OER activity with respect to Fe content is exhibited, with the lowest overpotential achieved on $Co_{1.33}Fe_{0.67}P_x$ (Co:Fe ratio of ~2:1). Adding more or less Fe decreases OER activity of NRs. The critical role of Fe may be contributed by its unique functionality in promoting the formation of active *O radical intermediate. ⁴³⁻⁴⁴ Recent

computational study of (Ni,Fe)OOH using state-of-the-art grand canonical quantum mechanics has indicated that, under high potential of OER condition, Fe is converted into Fe (IV) along with the deprotonation of absorbed *OH species, stabilizing the resultant *O radical intermediate. 45 The *O reacts with H₂O, allowing subsequent O-O coupling. According to theoretical calculation results, Fe (IV) is more efficient in stabilizing *O than other transition metals, while become less favorable for O-O coupling. This may explain the best activity of CNT-Co_{1.33}Fe_{0.67}P_x in our system, where Fe and Co surface sites provide two different functionalities essential to OER, forming an *O radical and catalyzing the O-O coupling, respectively. Fe outperforms other Ms in such a synergy with Co. Furthermore, the balanced ratio of Fe and Co contents in the case of Co_{1,33}Fe_{0.67}P_x makes it possible to maximize the synergetic cooperation between Co and Fe.

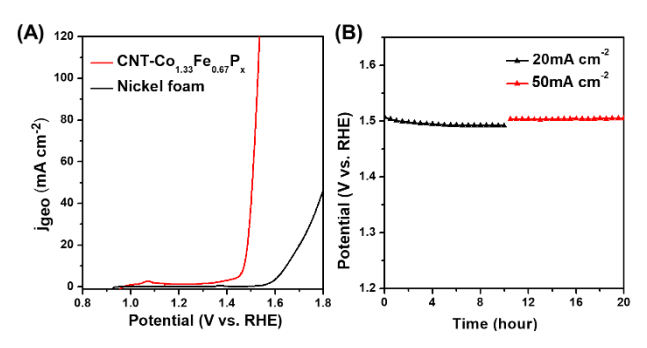


Figure 7. (A) OER polarization curves of pure nickel foam and the one modified with CNT-Co_{1.33}Fe_{0.67}P_x NRs. **(B)** Chronopotentiometry test of nickel foam modified with CNT-Co_{1.33}Fe_{0.67}P_x NRs. All electrochemical tests were performed in 1.0 M KOH.

The CNT-Co_{1.33}Fe_{0.67}P_x NRs were also loaded onto largearea Ni foam electrode for mimicking a practical device condition with large current densities (Fig. S23).46 As shown in Fig. 7A, the CNT-Co_{1.33}Fe_{0.67}P_x catalyst delivers an excellent OER activity, with a η =299 mV at 100 mA cm_{Geo}⁻¹. The long-term stability was evaluated via chronopotentiometries at 20 mA cm_{Geo}-2 for 10 hours, followed by another 10-hour testing at 50 mA cm_{Geo}⁻². As illustrated in Fig. 7B, the CNT-Co_{1.33}Fe_{0.67}P_x exhibits an activation stage with a slight decrease in the overpotential at the beginning of stability test, and presents a stable water oxidation afterwards with negligible change of overpotential. The activation stage is associated with the electrochemical surface oxidation. It is widely recognized that metal or metal phosphides can be further oxidized in the surface under oxygen electrochemistry conditions, in addition to the oxidation caused by air exposure. 47-⁵⁰ After the stabilization of the surface oxide layer, the Co_{1.33}Fe_{0.67}P_x catalyst becomes highly stable without any activity decay in the testing. The STEM-HAADF image and EELS 2-D elemental mapping of catalyst after the stability test indicate that the NR maintained the 1-D morphology with phosphide/oxide core/shell structure. (Fig. S24). The underlying phosphide core is a critical enabler for the excellent OER performance. It can improve the electrical conductivity, which is a common issue for oxide-based electrocatalysts. 40, 47, 51 Meanwhile, the 1-D structure of the NRs can provide a larger contiguous area to the supporting materials

and is thus beneficial to enhance the catalyst-support interaction, mitigating the migration-induced nanocatalyst agglomeration and activity decay. $^{52-53}$ These structural factors, plus the Fe and Co synergy, make $\text{Co}_{1.33}\text{Fe}_{0.67}P_x$ NRs highly efficient for OER catalysis.

4. CONCLUSION

In summary, we have developed a robust synthetic approach to producing multimetallic phosphide CoMP_x NRs with a uniform 1-D structure as well as programmable chemical composition. We found that using a two-stage synthesis, mediated by Co₂P/MP_x core/shell NRs formation and subsequent conversion, is the key to minimizing the NCs morphology and structure inconsistencies across a broad-range of bimetallic and trimetallic compositions, which is not otherwise accessible through conventional methods. The morphology uniformity and the composition tunability of CoMP_x NRs set a unique arena to accurately refine the composition-activity relationship for catalysis. Supported on CNT, the resultant CoMP_x NRs show M composition and concentration dependent electrocatalytic properties for the OER, with the best activity being achieved on $Co_{1.33}Fe_{0.67}P_x$. Given the wide adaptability presented by this method with diverse supporting materials (carbon materials and metal oxides), new opportunities can be expected to optimize these multimetallic phosphide NRs for other electrocatalytic and thermocatalytic reactions and beyond.

ASSOCIATED CONTENT

Supporting Information

Table S1. Figures S1-S24. This material is available free of charge via the Internet at http://pubs.acs.org.

AUTHOR INFORMATION

Corresponding Author

* sz3t@virginia.edu

ORCID

Zhiyong Zhang: 0000-0001-7936-9510 Hua Zhou: 0000-0001-9642-8674 Dong Su: 0000-0002-1921-6683 Sen Zhang: 0000-0002-1716-3741

Author Contributions

*These authors contributed equally to this work.

Notes

The authors declare no competing financial interest.

ACKNOWLEDGMENT

This work was supported by the U.S. National Science Foundation (DMR-1809700). Partial work on electron microscopy was carried out at the Center for Functional Nanomaterials, which is a U.S. Department of Energy Office of

Science Facility, at Brookhaven National Laboratory under Contract No. DE-SC0012704. Part of this research used resources [QAS, 7-BM] of the National Synchrotron Light Source II, a U.S. Department of Energy (DOE) Office of Science User Facility operated for the DOE Office of Science by Brookhaven National Laboratory under Contract No. DE-SC0012704. This research used resources of the Advanced Photon Source, a U.S. Department of Energy (DOE) Office of Science User Facility operated for the DOE Office of Science by Argonne National Laboratory under Contract No. DE-AC02-06CH11357.

REFERENCES

- 1. Carenco, S.; Portehault, D.; Boissiere, C.; Mezailles, N.; Sanchez, C., Nanoscaled Metal Borides and Phosphides: Recent Developments and Perspectives. *Chem. Rev.* **2013**, *113* (10), 7981-8065.
- 2. Brock, S. L.; Senevirathne, K., Recent Developments in Synthetic Approaches to Transition Metal Phosphide Nanoparticles for Magnetic and Catalytic Applications. *J. Solid State Chem.* **2008**, *181* (7), 1552-1559.
- 3. Anantharaj, S.; Ede, S. R.; Sakthikumar, K.; Karthick, K.; Mishra, S.; Kundu, S., Recent Trends and Perspectives in Electrochemical Water Splitting with an Emphasis on Sulfide, Selenide, and Phosphide Catalysts of Fe, Co, and Ni: A Review. *ACS Catalysis* **2016**, *6* (12), 8069-8097.
- 4. Popczun, E. J.; McKone, J. R.; Read, C. G.; Biacchi, A. J.; Wiltrout, A. M.; Lewis, N. S.; Schaak, R. E., Nanostructured nickel phosphide as an electrocatalyst for the hydrogen evolution reaction. *J. Am. Chem. Soc.* **2013**, *135* (25), 9267-70.
- 5. Xia, Y. Y., P.; Sun, Y.; Wu, Y.; Mayers, B.; Gates, B.; Yin, Y.; Kim, F.; Yan, H., One-Dimensional Nanostructures: Synthesis, Characterization, and Applications. *Adv. Mater.* **2003**, *15* (5), 353-389.
- 6. Zhang, Z.; Wu, Q.; Johnson, G.; Ye, Y.; Li, X.; Li, N.; Cui, M.; Lee, J. D.; Liu, C.; Zhao, S.; Li, S.; Orlov, A.; Murray, C. B.; Zhang, X.; Gunnoe, T. B.; Su, D.; Zhang, S., Generalized Synthetic Strategy for Transition-Metal-Doped Brookite-Phase TiO₂ Nanorods. *J. Am. Chem. Soc.* **2019**, *141* (42), 16548-16552.
- 7. Zhu, H.; Zhang, S.; Guo, S.; Su, D.; Sun, S., Synthetic Control of FePtM Nanorods (M = Cu, Ni) to Enhance the Oxygen Reduction Reaction. *J. Am. Chem. Soc.* **2013**, *135* (19), 7130-3.
- 8. Paik, T.; Cargnello, M.; Gordon, T. R.; Zhang, S.; Yun, H.; Lee, J. D.; Woo, H. Y.; Oh, S. J.; Kagan, C. R.; Fornasiero, P.; Murray, C. B., Photocatalytic Hydrogen Evolution from Substoichiometric Colloidal WO_{3-x} Nanowires. *ACS Energy Lett.* **2018**, *3* (8), 1904-1910.
- 9. Li, D.; Baydoun, H.; Verani, C. N.; Brock, S. L., Efficient Water Oxidation Using CoMnP Nanoparticles. *J. Am. Chem. Soc.* **2016**, *138* (12), 4006-9.
- 10. Mendoza-Garcia, A.; Zhu, H.; Yu, Y.; Li, Q.; Zhou, L.; Su, D.; Kramer, M. J.; Sun, S., Controlled Anisotropic Growth of Co-Fe-P from Co-Fe-O Nanoparticles. *Angew Chem. Int. Ed.* **2015**, *54* (33), 9642-5.
- 11. Read, C. G.; Callejas, J. F.; Holder, C. F.; Schaak, R. E., General Strategy for the Synthesis of Transition Metal

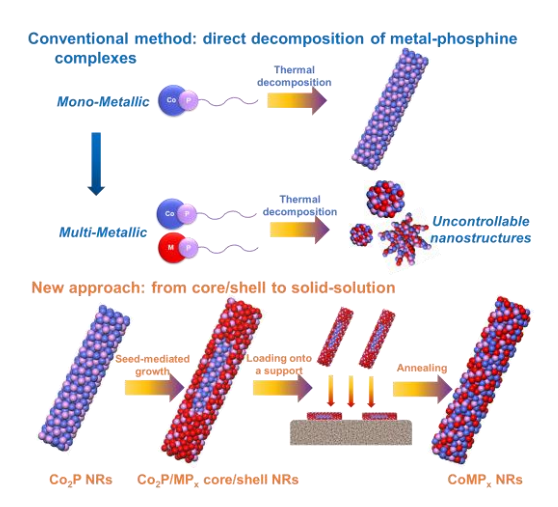
- Phosphide Films for Electrocatalytic Hydrogen and Oxygen Evolution. *ACS Appl. Mater. Interfaces.* **2016,** 8 (20), 12798-803.
- 12. Brock, S. L.; Perera, S. C.; Stamm, K. L., Chemical Routes for Production of Transition-Metal Phosphides on the Nanoscale: Implications for Advanced Magnetic and Catalytic Materials. *Chemistry* **2004**, *10* (14), 3364-71.
- 13. Su, J.; Zhou, J.; Wang, L.; Liu, C.; Chen, Y., Synthesis and Application of Transition Metal Phosphides as Electrocatalyst for Water Splitting. *Sci. Bull.* **2017**, *62* (9), 633-644.
- 14. Henkes, A. E. V., Y.; Schaak, R. E., Converting Metals into Phosphides: A General Strategy for the Synthesis of Metal Phosphide Nanocrystals. *J. Am. Chem. Soc.* **2007**, *129* (7), 1896-1897.
- 15. Li, D.; Arachchige, M. P.; Kulikowski, B.; Lawes, G.; Seda, T.; Brock, S. L., Control of Composition and Size in Discrete Co_xFe_{2-x}P Nanoparticles: Consequences for Magnetic Properties. *Chem. Mater.* **2016**, *28* (11), 3920-3927.
- 16. Chen, Y.; She, H.; Luo, X.; Yue, G.-H.; Peng, D.-L., Solution-Phase Synthesis of Nickel Phosphide Single-Crystalline Nanowires. *J. Cryst. Growth* **2009**, *311* (4), 1229-1233.
- 17. Park, J. K., B.; Yoon, K. Y.; Hwang, Y.; Kang, M.; Park, J. G., Hyeon, T., Generalized Synthesis of Metal Phosphide Nanorods via Thermal Decomposition of Continuously Delivered Metal-Phosphide Complexes Using a Syringe Pump. *J. Am. Chem. Soc.* **2005**, *127* (23), 8433-8440.
- 18. Doan-Nguyen, V. V. T. Z., S.; Trigg, E. B.; Agarwal, R.; Li, J.; Su, D.; Winey, K. I.; Murray, C. B., Synthesis and X-ray Characterization of Cobalt Phosphide (Co₂P) Nanorods for the Oxygen Reduction Reaction. *ACS Nano* **2015**, *9* (8), 8108–8115.
- 19. Qian, C. K., F.; Ma, L.; Tsui, F.; Yang, P.; Liu, J., Solution-Phase Synthesis of Single-Crystalline Iron Phosphide Nanorods/Nanowires. *J. Am. Chem. Soc.* **2003**, *126* (4), 1195-1198.
- 20. Gregg, K. A.; Perera, S. C.; Lawes, G.; Shinozaki, S.; Brock, S. L., Controlled Synthesis of MnP Nanorods: Effect of Shape Anisotropy on Magnetization. *Chem. Mater.* **2006,** *18* (4), 879-886.
- 21. Hitihami-Mudiyanselage, A.; Arachchige, M. P.; Seda, T.; Lawes, G.; Brock, S. L., Synthesis and Characterization of Discrete Fe_xNi_{2-x}P Nanocrystals (0 < x < 2): Compositional Effects on Magnetic Properties. *Chem. Mater.* **2015**, *27* (19), 6592-6600.
- 22. Liu, C.; Ma, Z.; Cui, M.; Zhang, Z.; Zhang, X.; Su, D.; Murray, C. B.; Wang, J. X.; Zhang, S., Favorable Core/Shell Interface within Co₂P/Pt Nanorods for Oxygen Reduction Electrocatalysis. *Nano Lett.* **2018**, *18* (12), 7870-7875.
- 23. Ma, Y.; Li, W.; Cho, E. C.; Li, Z. Y., T.; ; Zeng, J.; Xie, Z.; Xia, Y., Au@Ag Core—Shell Nanocubes with Finely Tuned and Well Controlled Sizes, Shell Thicknesses, and Optical Properties. *ACS Nano* **2010**, *4* (11), 6725-6734.
- 24. Zhang, J. T.; Tang, Y.; Lee, K.; Ouyang, M., Nonepitaxial Growth of Hybrid Core-Shell Nanostructures

- with Large Lattice Mismatches. Science 2010, 327, 1634-1638
- 25. Fan, Z.; Zhang, X.; Yang, J.; Wu, X.; Liu, Z.; Huang, W.; Zhang, H., Synthesis of 4H/fcc-Au@Metal Sulfide Core-Shell Nanoribbons. *J. Am. Chem. Soc.* **2015**, *137* (34), 10910-10913.
- 26. Zhang, X.; Yu, X.; Zhang, L.; Zhou, F.; Liang, Y.; Wang, R., Molybdenum Phosphide/Carbon Nanotube Hybrids as pH-Universal Electrocatalysts for Hydrogen Evolution Reaction. *Adv. Funct. Mater.* **2018**, *28* (16), 1706523.
- 27. Parra-Puerto, A.; Ng, K. L.; Fahy, K.; Goode, A. E.; Ryan, M. P.; Kucernak, A., Supported Transition Metal Phosphides: Activity Survey for HER, ORR, OER, and Corrosion Resistance in Acid and Alkaline Electrolytes. *ACS Catalysis* **2019**, *9* (12), 11515-11529.
- 28. Enache, D. I., Edwards, J. K., Landon, P., Solsona-Espriu, B., Carley, A. F., Herzing, A. A., Watanabe, M., Kiely, C. J., Knight, D. W., Hutchings, G. J., Solvent-Free Oxidation of Primary Alcohols to Aldehydes Using Au-Pd/TiO₂ Catalysts. *Science* **2006**, *311* (5759), 362-365.
- 29. Ting, K. W.; Toyao, T.; Siddiki, S. M. A. H.; Shimizu, K.-i., Low-Temperature Hydrogenation of CO₂ to Methanol over Heterogeneous TiO₂-Supported Re Catalysts. *ACS Catalysis* **2019**, *9* (4), 3685-3693.
- 30. Onn, T. M.; Zhang, S.; Arroyo-Ramirez, L.; Chung, Y.-C.; Graham, G. W.; Pan, X.; Gorte, R. J., Improved Thermal Stability and Methane-Oxidation Activity of Pd/Al₂O₃ Catalysts by Atomic Layer Deposition of ZrO₂. *ACS Catalysis* **2015**, *5* (10), 5696-5701.
- 31. Yu, J.; Li, Q.; Li, Y.; Xu, C.-Y.; Zhen, L.; Dravid, V. P.; Wu, J., Ternary Metal Phosphide with Triple-Layered Structure as a Low-Cost and Efficient Electrocatalyst for Bifunctional Water Splitting. *Adv. Funct. Mater.* **2016**, *26* (42), 7644-7651.
- 32. Li, P.; Zeng, H. C., Promoting Electrocatalytic Oxygen Evolution over Transition-Metal Phosphide-Based Nanocomposites via Architectural and Electronic Engineering. *ACS Appl. Mater. Interfaces* **2019**, *11* (50), 46825-46838.
- 33. Moreau, L. M.; Ha, D.-H.; Zhang, H.; Hovden, R.; Muller, D. A.; Robinson, R. D., Defining Crystalline/Amorphous Phases of Nanoparticles through X-ray Absorption Spectroscopy and X-ray Diffraction: The Case of Nickel Phosphide. *Chem. Mater.* **2013**, *25* (12), 2394-2403.
- 34. Zhang, Z.; Liu, C.; Brosnahan, J. T.; Zhou, H.; Xu, W.; Zhang, S., Revealing structural evolution of PbS nanocrystal catalysts in electrochemical CO₂ reduction using in situ synchrotron radiation X-ray diffraction. *J. Mater. Chem. A.* **2019**, *7* (41), 23775-23780.
- 35. Kim, H.; Oh, S.; Cho, E.; Kwon, H., 3D Porous Cobalt–Iron–Phosphorus Bifunctional Electrocatalyst for the Oxygen and Hydrogen Evolution Reactions. *ACS Sustainable Chem. Eng.* **2018**, *6* (5), 6305-6311.
- 36. Xu, J.; Li, J.; Xiong, D.; Zhang, B.; Liu, Y.; Wu, K. H.; Amorim, I.; Li, W.; Liu, L., Trends in Activity for the Oxygen Evolution Reaction on Transition Metal (M = Fe, Co, Ni) Phosphide Pre-Catalysts. *Chem. Sci.* **2018**, *9* (14), 3470-3476.

- 37. Liang, H.; Gandi, A. N.; Anjum, D. H.; Wang, X.; Schwingenschlogl, U.; Alshareef, H. N., Plasma-Assisted Synthesis of NiCoP for Efficient Overall Water Splitting. *Nano Lett.* **2016**, *16* (12), 7718-7725.
- 38. Kanda, Y.; Kawanishi, K.; Tsujino, T.; Al-otaibi, A.; Uemichi, Y., Catalytic Activities of Noble Metal Phosphides for Hydrogenation and Hydrodesulfurization Reactions. *Catalysts* **2018**, *8* (4), 160-171.
- 39. Oyama, S. T.; Lee, Y., Mechanism of Hydrodenitrogenation on Phosphides and Sulfides. *J. Phys. Chem.* **2005**, *109* (6), 2109-2119.
- 40. Callejas, J. F.; Read, C. G.; Roske, C. W.; Lewis, N. S.; Schaak, R. E., Synthesis, Characterization, and Properties of Metal Phosphide Catalysts for the Hydrogen-Evolution Reaction. *Chem. Mater.* **2016**, *28* (17), 6017-6044.
- 41. Li, D.; Baydoun, H.; Kulikowski, B.; Brock, S. L., Boosting the Catalytic Performance of Iron Phosphide Nanorods for the Oxygen Evolution Reaction by Incorporation of Manganese. *Chem. Mater.* **2017**, *29* (7), 3048-3054.
- 42. Gao, M. R.; Xu, Y. F.; Jiang, J.; Zheng, Y. R.; Yu, S. H., Water Oxidation Electrocatalyzed by an Efficient Mn₃O₄/CoSe₂ Nanocomposite. *J. Am. Chem. Soc.* **2012**, *134* (6), 2930-3.
- 43. Martirez, J. M. P.; Carter, E. A., Unraveling Oxygen Evolution on Iron-Doped beta-Nickel Oxyhydroxide: The Key Role of Highly Active Molecular-like Sites. *J. Am. Chem. Soc.* **2019**, *141* (1), 693-705.
- 44. Burke, M. S.; Kast, M. G.; Trotochaud, L.; Smith, A. M.; Boettcher, S. W., Cobalt-Iron (Oxy)hydroxide Oxygen Evolution Electrocatalysts: the Role of Structure and Composition on Activity, Atability, and Mechanism. *J. Am. Chem. Soc.* **2015**, *137* (10), 3638-48.
- 45. Xiao, H.; Shin, H.; Goddard, W. A., 3rd, Synergy between Fe and Ni in the Optimal Performance of (Ni,Fe)OOH Catalysts for the Oxygen Evolution Reaction. *Proc. Natl. Acad. Sci. USA* **2018**, *115* (23), 5872-5877.
- 46. You, B.; Jiang, N.; Sheng, M.; Bhushan, M. W.; Sun, Y., Hierarchically Porous Urchin-Like Ni₂P

- Superstructures Supported on Nickel Foam as Efficient Bifunctional Electrocatalysts for Overall Water Splitting. *ACS Catalysis* **2015**, *6* (2), 714-721.
- 47. Dutta, A.; Pradhan, N., Developments of Metal Phosphides as Efficient OER Precatalysts. *J. Phys. Chem. Lett.* **2017**, *8* (1), 144-152.
- 48. Wygant, B. R.; Kawashima, K.; Mullins, C. B., Catalyst or Precatalyst? The Effect of Oxidation on Transition Metal Carbide, Pnictide, and Chalcogenide Oxygen Evolution Catalysts. *ACS Energy Lett.* **2018**, *3* (12), 2956-2966.
- 49. Duan, Y.; Yu, Z. Y.; Hu, S. J.; Zheng, X. S.; Zhang, C. T.; Ding, H. H.; Hu, B. C.; Fu, Q. Q.; Yu, Z. L.; Zheng, X.; Zhu, J. F.; Gao, M. R.; Yu, S. H., Scaled-Up Synthesis of Amorphous NiFeMo Oxides and Their Rapid Surface Reconstruction for Superior Oxygen Evolution Catalysis. *Angew. Chem. Int. Ed.* **2019**, *58*, 15772-15777.
- 50. Jin, S., Are Metal Chalcogenides, Nitrides, and Phosphides Oxygen Evolution Catalysts or Bifunctional Catalysts? *ACS Energy Letters* **2017**, *2* (8), 1937-1938.
- 51. Blanchard, P. E. R.; Grosvenor, A. P.; G.;, C. R.; Mar, A., X-ray Photoelectron and Absorption Spectroscopy of Metal-Rich Phosphides M₂P and M₃P (M=Cr-Ni). *Chem. Mater.* **2008**, *20* (22), 7081–7088.
- 52. Li, K.; Li, X.; Huang, H.; Luo, L.; Li, X.; Yan, X.; Ma, C.; Si, R.; Yang, J.; Zeng, J., One-Nanometer-Thick PtNiRh Trimetallic Nanowires with Enhanced Oxygen Reduction Electrocatalysis in Acid Media: Integrating Multiple Advantages into One Catalyst. *J. Am. Chem. Soc.* **2018**, *140* (47), 16159-16167.
- 53. Hang, H. L., K.; Chen, Z.; Luo, L.; Gu, Y.; Zhang, D.; Ma, C.; Si, R.; Yang, J.; Peng, Z.; Zeng, J., Achieving Remarkable Activity and Durability toward Oxygen Reduction Reaction Based on Ultrathin Rh-Doped Pt Nanowires. *J. Am. Chem. Soc.* **2017**, *139* (24), 8152-8159.

TOC



Supporting Information

Programmable Synthesis of Multimetallic Phosphide Nanorods Mediated by Core/Shell Structure Formation and Conversion

Yulu Zhang, † Na Li, ‡, # Zhiyong Zhang, † Shuang Li, ‡ Meiyang Cui, † Lu Ma, § Hua Zhou, ^ Dong Su, ‡ Sen Zhang*, †

E-mail for S. Z.: sz3t@virginia.edu

Contents:

This file includes Supplementary Table S1, and Supplementary Figure S1-S24.

[†] Department of Chemistry, University of Virginia, Charlottesville, Virginia 22904, United States;

[‡] Center for Functional Nanomaterials, Brookhaven National Laboratory, Upton, New York 11973, United States;

[§] National Synchrotron Light Source II, Brookhaven National Laboratory, Upton, New York 11973, United States;

[△] X-ray Science Division, Advanced Photon Source, Argonne National Laboratory, Lemont, Illinois 60439, United States;

^{*}To whom correspondence should be addressed.

Table of Contents

Suppl	lementary	Tables
-------	-----------	---------------

Table S1. Co ₂ P/metal precursor ratios and ICP results.	S3
Supplementary Figures	
Figure S1. TEM images of CoNiP _x NCs.	S4
Figure S2. TEM images of CoFeP _x , CoMnP _x , and CoCuP _x NCs	S4
Figure S3. TEM images of Co ₂ P NRs (24.7nm)	S5
Figure S4. TEM image of Co ₂ P/FeP _x (1:3) NRs	S5
Figure S5. TEM images of Co ₂ P/NiP _x , Co ₂ P/MnP _x and Co ₂ P/CuP _x NRs	S6
Figure S6. HAADF-STEM images of Co ₂ P/NiP _x (2:1) NRs.	S7
Figure S7. HAADF-STEM images of Co ₂ P/FeP _x (2:1) NRs	S7
Figure S8. EELS line scans of Co ₂ P/FeP _x and Co ₂ P/MnP _x NRs	S8
Figure S9. TEM images of Co ₂ P/NiFeP _x (Co:Ni:Fe=2:1:1) and Co ₂ P/NiMnP _x (Co:Ni:Mn=3:1:1) NRs	S8
Figure S10. STEM-EELS elemental mappings of CNTs-Co _{1.01} Ni _{0.43} Fe _{0.56} P _x	S9
Figure S11. HAADF-STEM images of CNT-Co _{1.30} Ni _{0.70} P _x NRs	S9
Figure S12. TEM images of Co _{1.30} Ni _{0.70} P _x NRs on Vulcan-72 carbon black, Al ₂ O ₃ and TiO ₂	S10
Figure S13. SRXRD patterns of C-Co ₂ P NRs (36.5 nm)	S10
Figure S14 . XPS survey scans of C-Co ₂ P/FeP _x (2:1), C-Co _{1.33} Fe _{0.67} P _x and C-Co _{1.01} Fe _{0.43} Ni _{0.56} P _x NRs	S11
Figure S15. High resolution XPS spectra of C-Co ₂ P NRs (36.5 nm)	S11
Figure S16. High resolution XPS spectra of C-Co _{1.10} Fe _{0.90} P _x NRs.	S11
Figure S17. High resolution XPS spectra of C-Co _{1.30} Ni _{0.70} P _x NRs.	S12
Figure S18. High resolution XPS spectra of C-Co _{1.25} Mn _{0.75} P _x NRs.	S12
Figure S19. High resolution XPS spectra of C-Co _{1.25} Cu _{0.75} P _x NRs	S12
Figure S20. High resolution XPS spectra of C-Co _{1.01} Ni _{0.43} Fe _{0.56} P _x NRs.	S13
Figure S21. OER polarization curve of CNT-Co ₂ P NRs (36.5 nm), compared with GC and CNTs	S13
Figure S22. Tafel slopes for C-Co ₂ P, -Co _{1.45} Fe _{0.55} P _x , -Co _{1.33} Fe _{0.67} P _x , -Co _{1.10} Fe _{0.90} P _x and -Co _{0.54} Fe _{1.46} P _x , -Co _{1.25} Mn _{0.75} P _x and -Co _{1.25} Cu _{0.75} P _x NRs.	
Figure S23. SEM images of CNT-Co _{1.33} Fe _{0.67} P _x NRs pasted on nickel foam.	S14
Figure S24. STEM-HAADF image and EELS 2-D elemental mappings of CNTs-Co _{1.33} Fe _{0.67} P _x NRs after the test.	ne stability

Table S1. Quantities of Co_2P seeds (36.5 nm) and metal precursors for the synthesis of Co_2P/MP_x NRs and $Co_2P/M_1M_2P_x$.

Co ₂ P/MP _x	Reactants	Co:M (Expected)	Co ₂ P seeds	M(acac) _x	Co:M (ICP result)
		(Expecteu)			(ICI Tesuit)
Co ₂ P/NiP _x	Ni(acac) ₂	1:1	40 mg	0.12 mmol	0.83:1
		2:1	40 mg	0.06 mmol	1.86:1
		3:1	80 mg	0.08 mmol	3.36:1
Co ₂ P/FeP _x	Fe(acac) ₃	1:3	20 mg	0.23 mmol	1:2.72
		1:1	20 mg	0.13 mmol	1.22:1
		2:1	40 mg	0.11 mmol	1.99:1
		3:1	40 mg	0.10 mmol	2.63:1
Co ₂ P/MnP _x	Mn(acac) ₂	1:1	20 mg	0.16 mmol	1.22:1
		2:1	40 mg	0.16 mmol	1.68:1
		3:1	40 mg	0.10 mmol	3.32:1
Co ₂ P/CuP _x	Cu(acac) ₂	1:1	20 mg	0.20 mmol	0.95:1
		2:1	40 mg	0.12 mmol	1.67:1
		3:1	40 mg	0.06 mmol	2.96:1
Co ₂ P/NiFeP _x	Ni(acac) ₂	2:1	40	0.08 mmol	2.34:1
	+ Fe(acac) ₃	2:1	40 mg	0.11 mmol	1.83:1
Co ₂ P/NiMnP _x	Ni(acac) ₂	3:1	40 .	0.10 mmol	2.96:1
	+ Mn(acac) ₂	3:1	40 mg	0.20 mmol	2.83:1

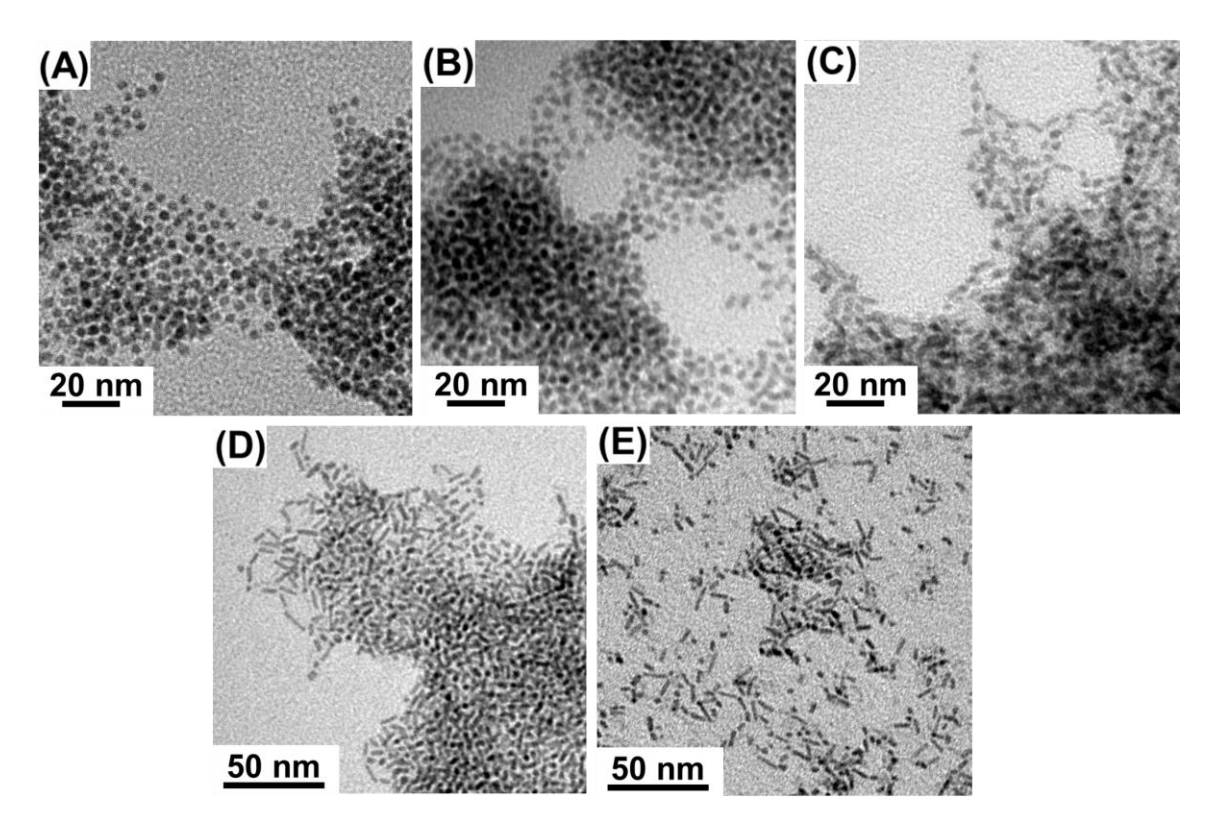


Figure S1. (A-E) TEM images of CoNiP_x NCs synthesized via the co-decomposition of Co- and Ni-TBP complexes. The Co:Ni precursor ratio is controlled to be (A) 1:1, (B) 4:1, (C) 9:1, (D) 14:1, (E) 19:1.

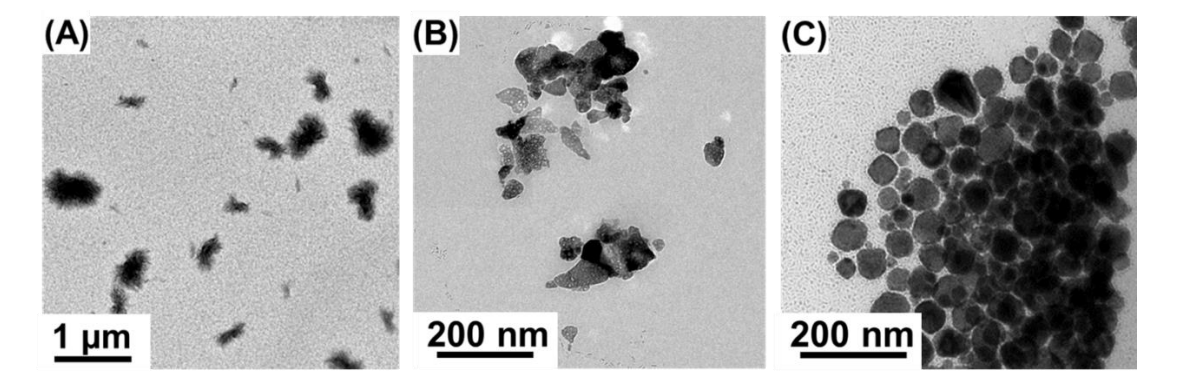


Figure S2. (A-C) TEM images of (A) CoFeP_x, (B) CoMnP_x, and (C) CoCuP_x NCs synthesized via the co-decomposition of Co- and M-TBP complexes. The Co:M precursor ratio is controlled to be 1:1.

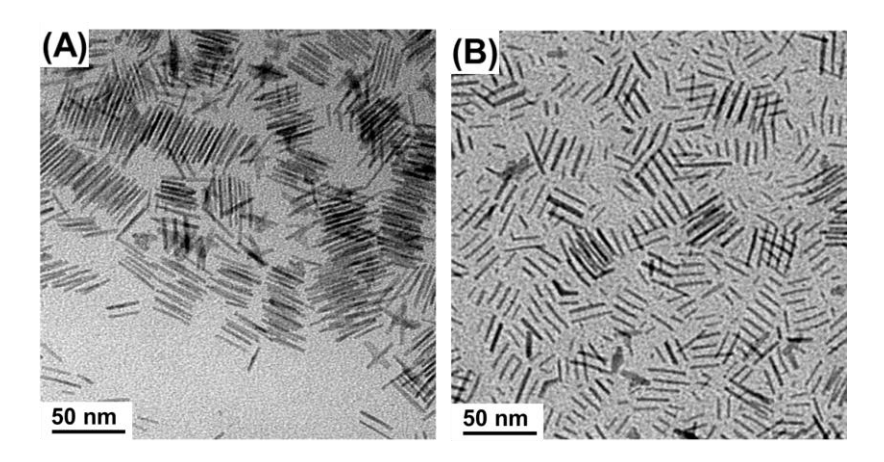


Figure S3. TEM images of Co₂P NRs synthesized at 260°C in (A) BE and (B) ODE.

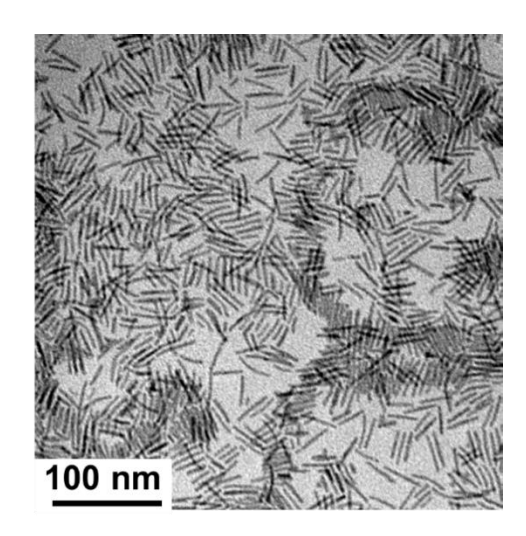


Figure S4. TEM image of Co_2P/FeP_x core/shell NRs with Co:Fe ratio of $\sim 1:3$, using 36.5 nm Co_2P seeds

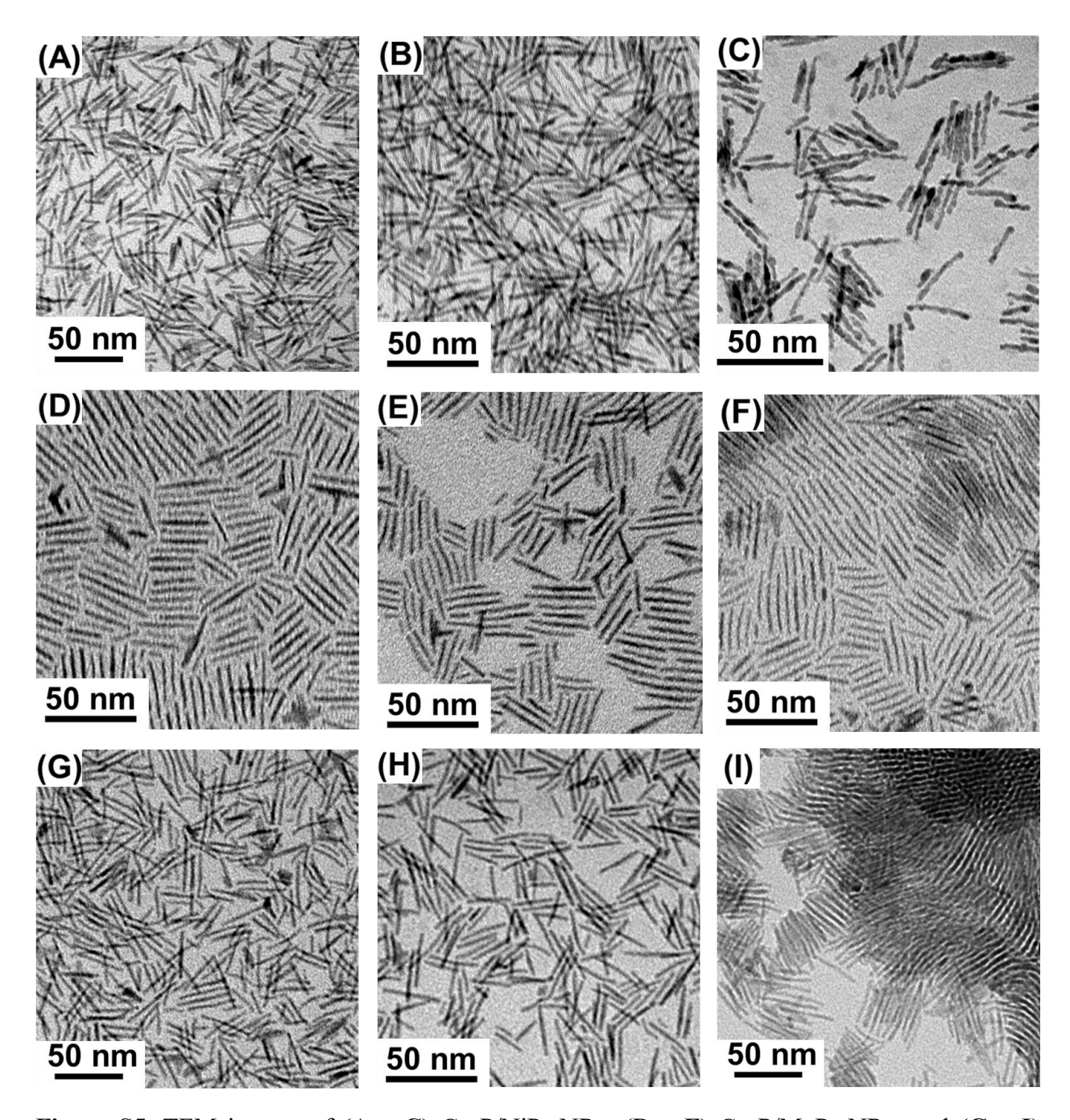


Figure S5. TEM images of (A - C) Co₂P/NiP_x NRs; (D - F) Co₂P/MnP_x NRs; and (G - I) Co₂P/CuP_x NRs. The Co:M ratios are $\sim (A, D, G)$ 3:1; (B, E, H) 2:1; and (C, F, I) 1:1. All syntheses were carried out using 36.5 nm Co₂P seeds.

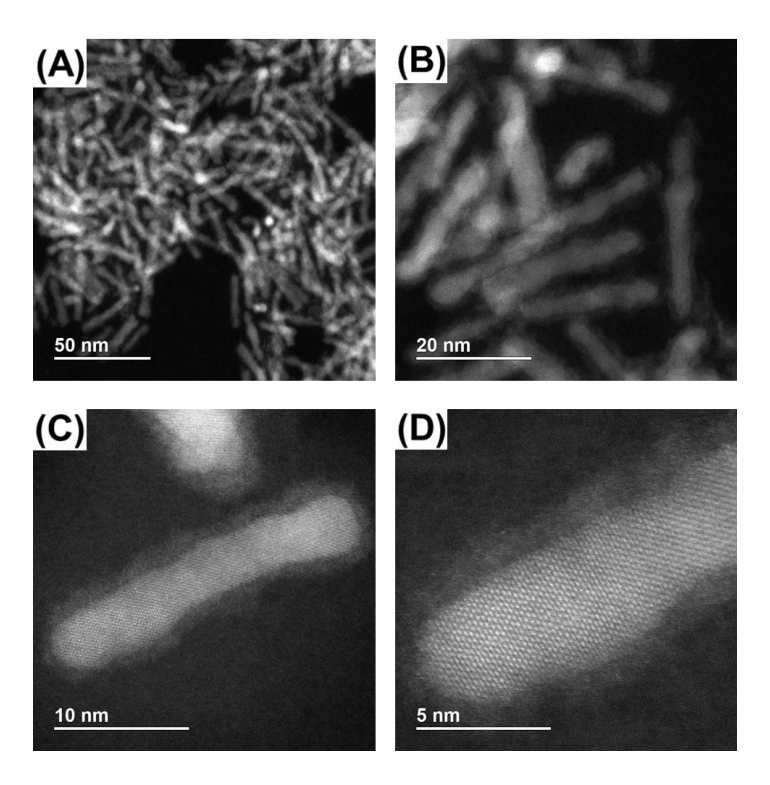


Figure S6. HAADF-STEM images of Co_2P/NiP_x NRs using 24.7 nm Co_2P seeds and Co:Ni ratio of $\sim 2:1$, at different magnifications.

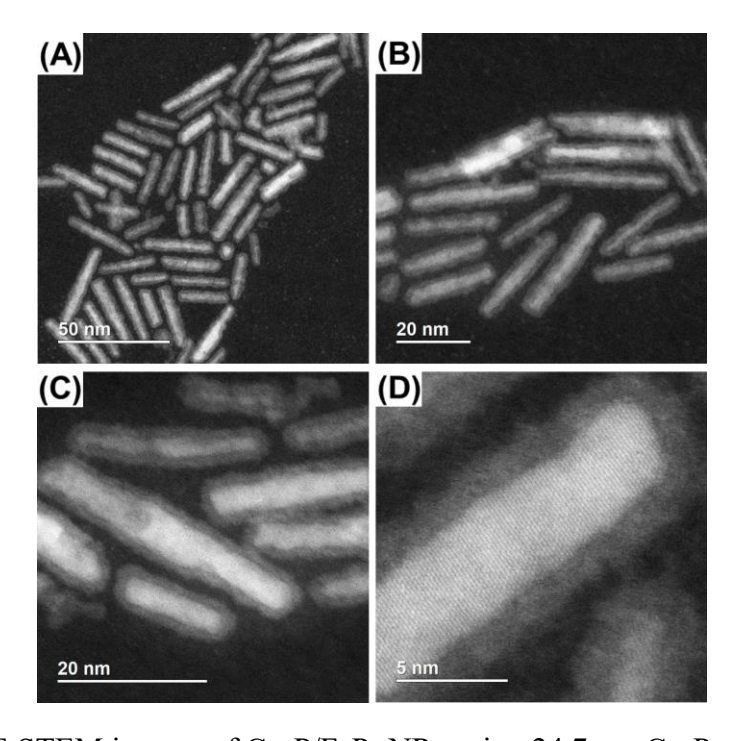


Figure S7. HAADF-STEM images of Co_2P/FeP_x NRs using 24.7 nm Co_2P seeds and Co:Fe ratio of $\sim 2:1$, at different magnifications.

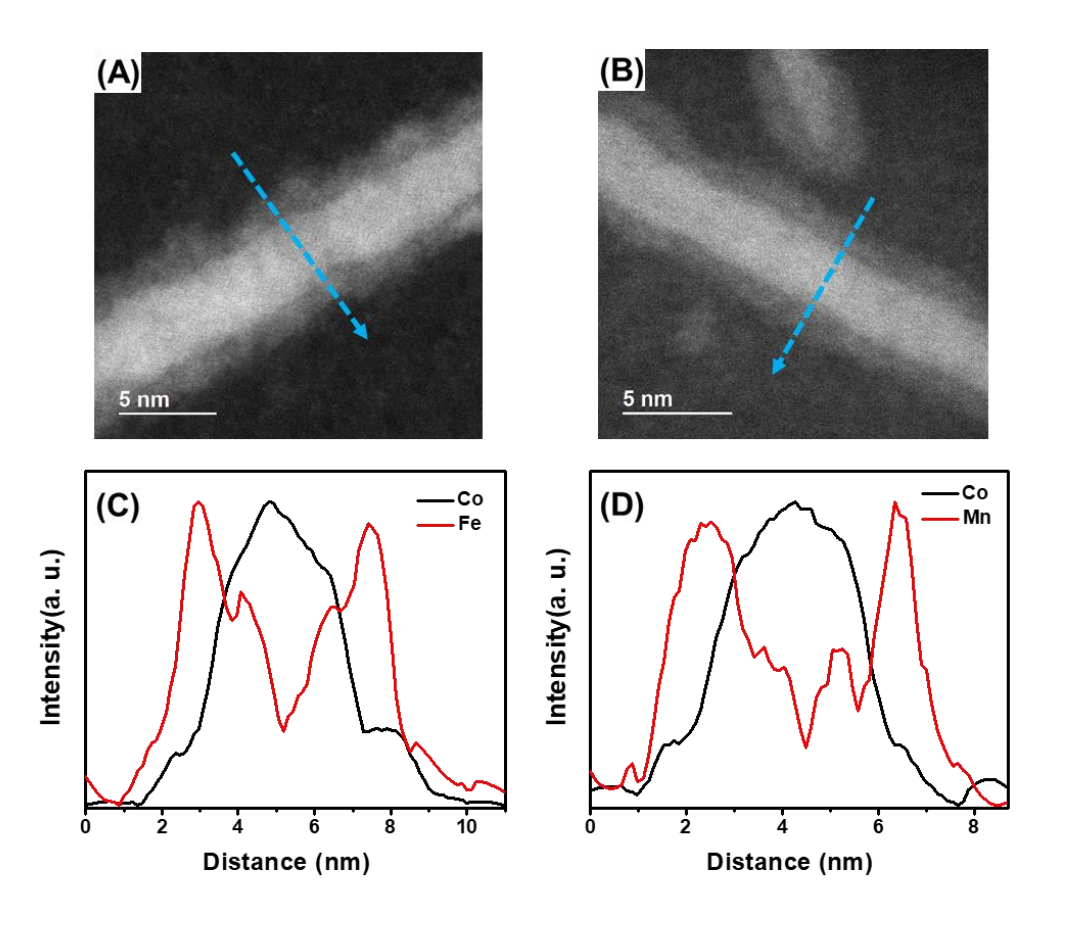


Figure S8. HAADF-STEM coupled with EELS line scans of (A, C) Co_2P/FeP_x ; and (B, D) Co_2P/MnP_x NRs. Syntheses were carried out using 36.5 nm Co_2P seeds with Co:M atomic ratio of $\sim 2:1$.

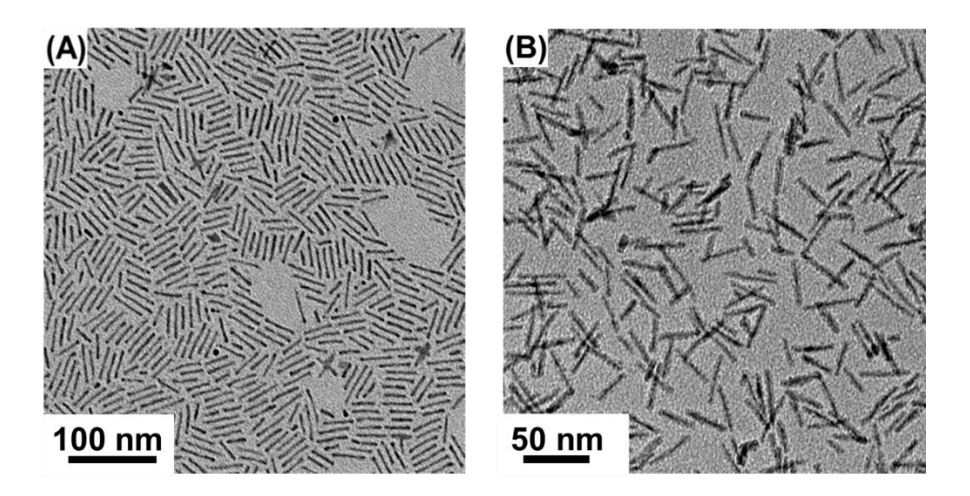


Figure S9. TEM images of trimetallic **(A)** $Co_2P/NiFeP_x$ (Co:Ni:Fe ratio is ~2:1:1), and **(B)** $Co_2P/NiMnP_x$ (Co:Ni:Mn ratio is ~3:1:1). Syntheses were carried out using 36.5 nm Co_2P seeds.

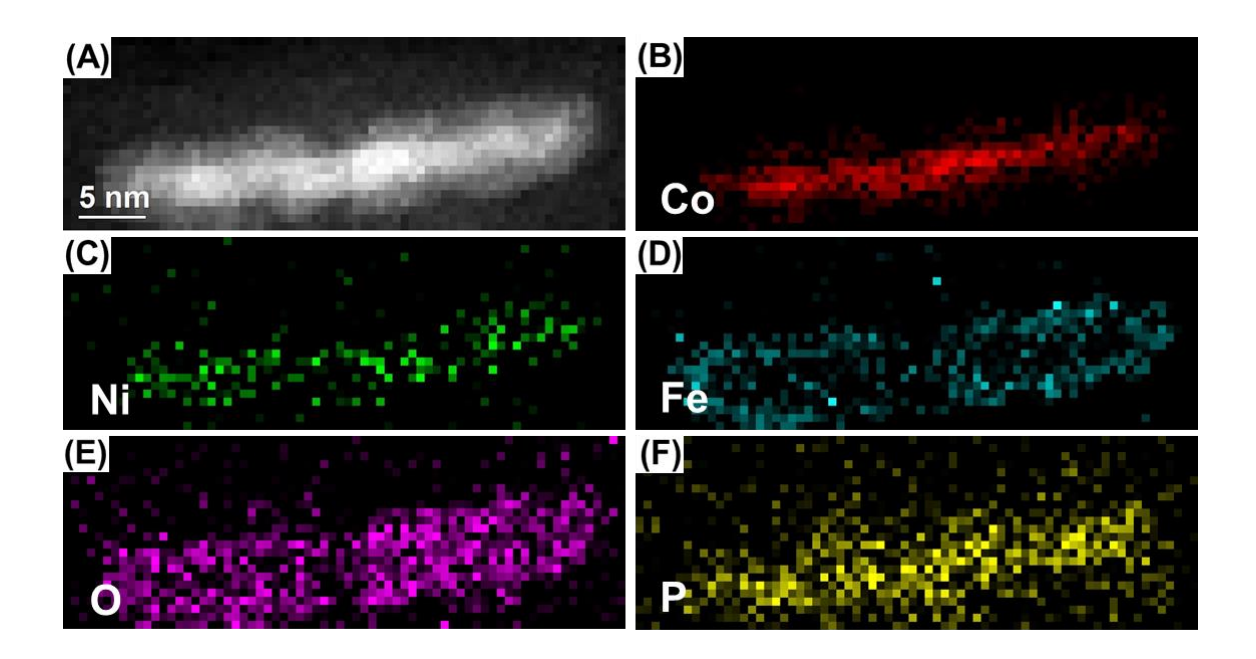


Figure S10. STEM-EELS elemental mapping of CNT-Co_{1.01}Ni_{0.43}Fe_{0.56}P_x, using 36.5 nm Co₂P seeds.

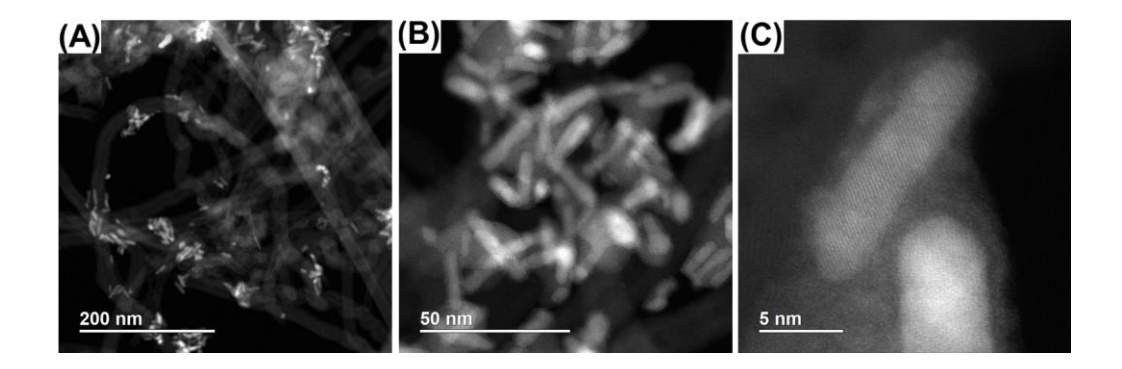


Figure S11. HAADF-STEM images of CNT-Co_{1.30}Ni_{0.70}P_x NRs, using 24.7 nm Co₂P seeds.

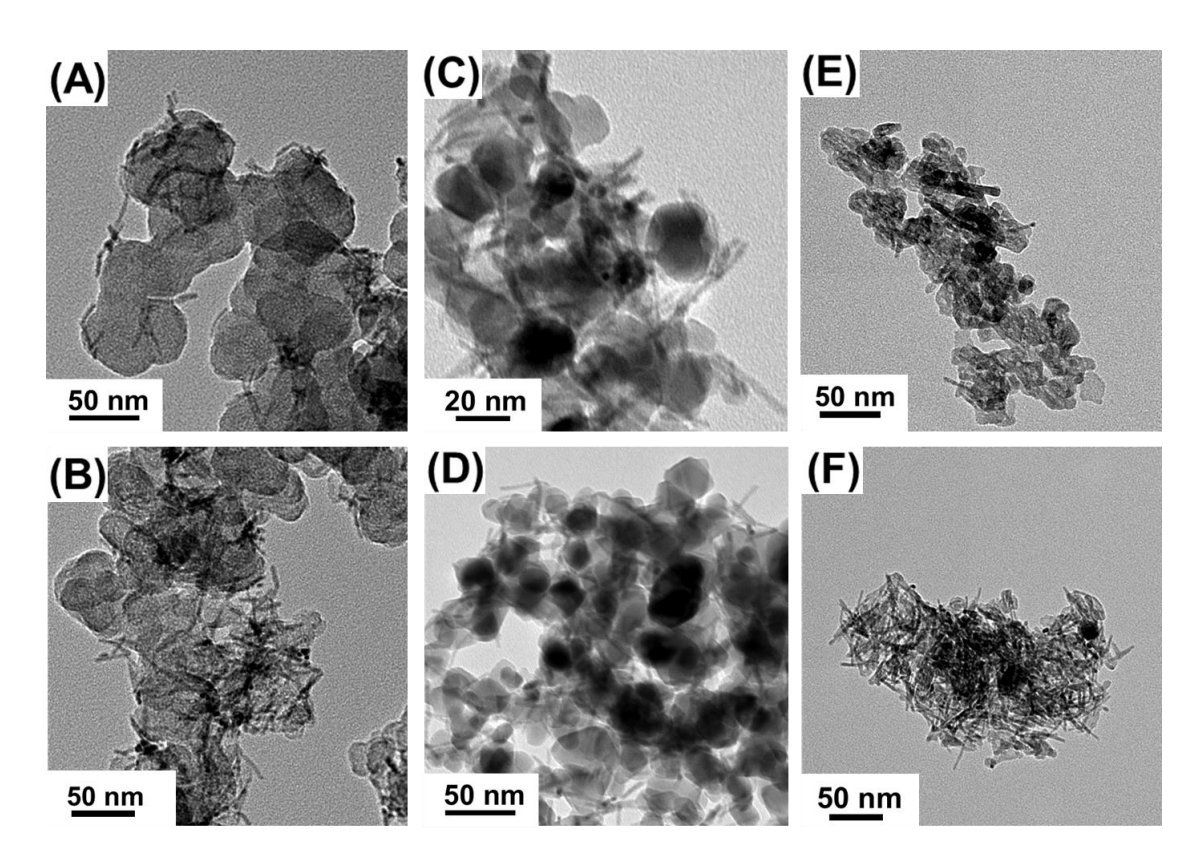


Figure S12. TEM images of $Co_{1.30}Ni_{0.70}P_x$ NRs supported and annealed on **(A-B)** Vulcan-72 carbon black; **(C-D)** Al_2O_3 ; and **(E-F)** TiO_2 (P25) in forming gas at 400°C for 2 hour. Syntheses were carried out using 36.5 nm Co_2P seeds.

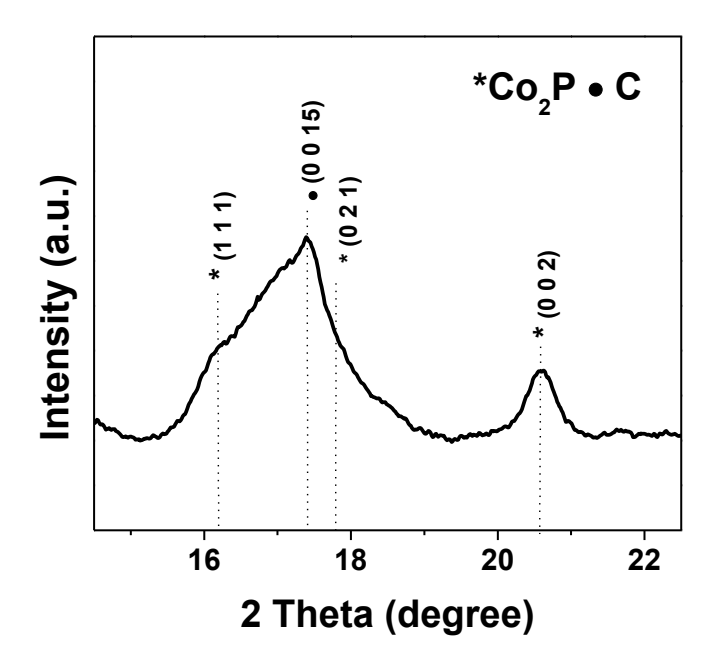


Figure S13. SR-XRD pattern of C-Co₂P NRs (36.5 nm).

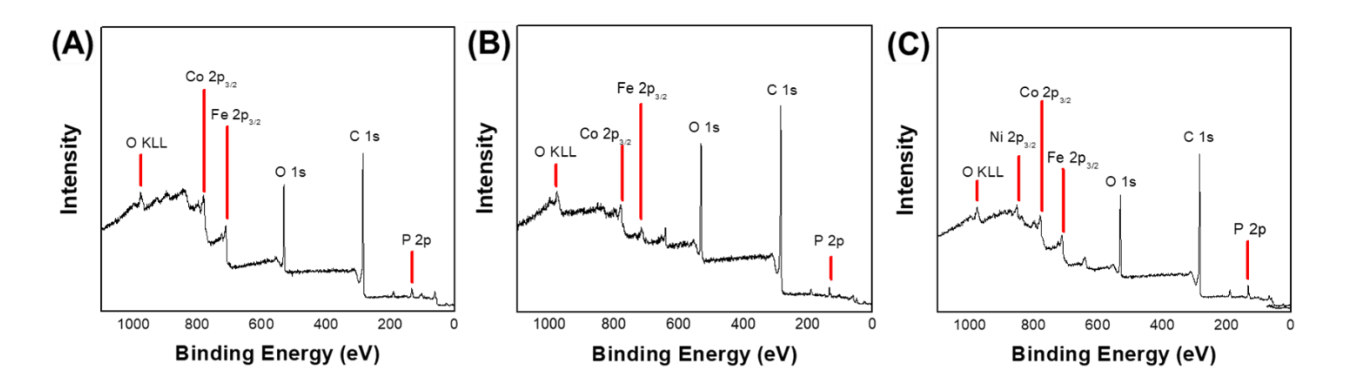


Figure S14. XPS survey scans of **(A)** C-Co₂P/FeP_x (Co:Fe ratio of ~2:1); **(B)** C-Co_{1.33}Fe_{0.67}P_x; **(C)** C-Co_{1.01}Fe_{0.43}Ni_{0.56}P_x NRs. (B, C) are samples after annealing. Syntheses were carried out using 36.5 nm Co₂P seeds.

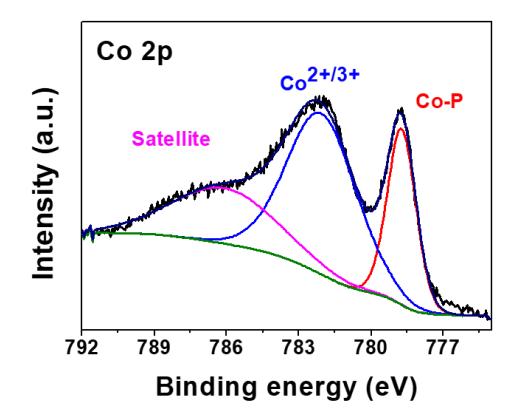


Figure S15. High resolution Co 2p XPS spectrum of C-Co₂P NRs (36.5 nm).

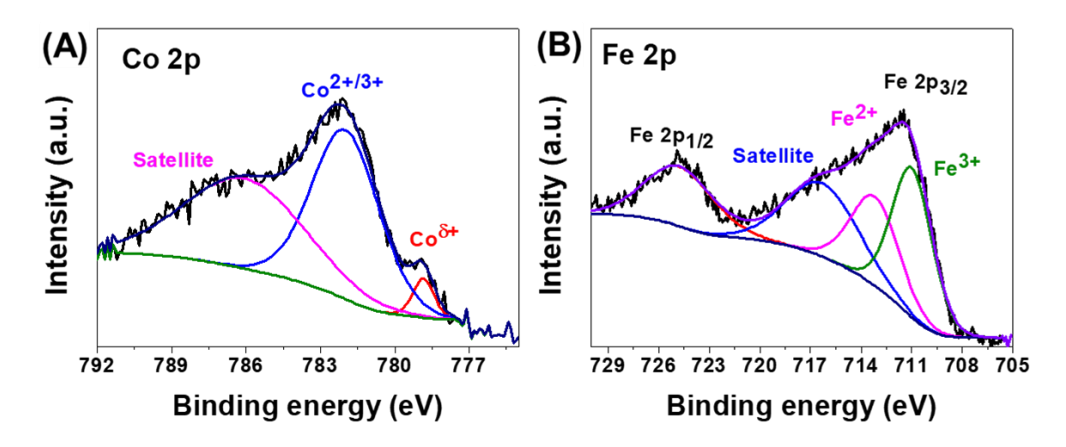


Figure S16. High resolution XPS spectra of **(A)** Co 2p and **(B)** Fe 2p of C-Co_{1.10}Fe_{0.90}P_x NRs, using 36.5 nm Co₂P seeds.

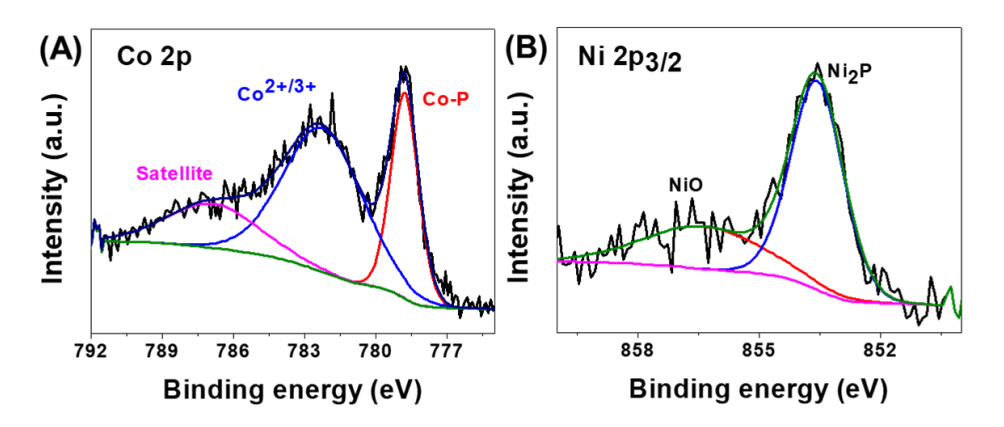


Figure S17. High resolution XPS spectra of **(A)** Co 2p and **(B)** Ni 2p of C-Co_{1.30}Ni_{0.70}P_x NRs, using 36.5 nm Co₂P seeds.

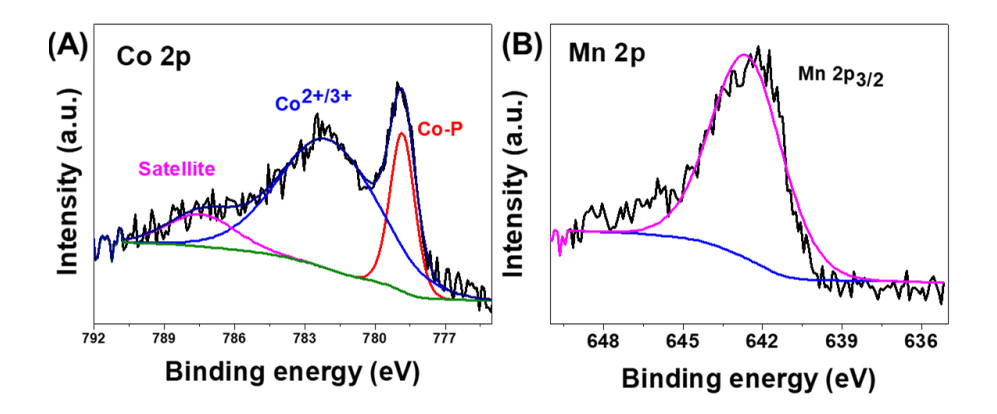


Figure S18. High resolution XPS spectra of (A) Co 2p and (B) Mn 2p of C-Co_{1.25}Mn_{0.75}P_x NRs, using 36.5 nm Co₂P seeds.

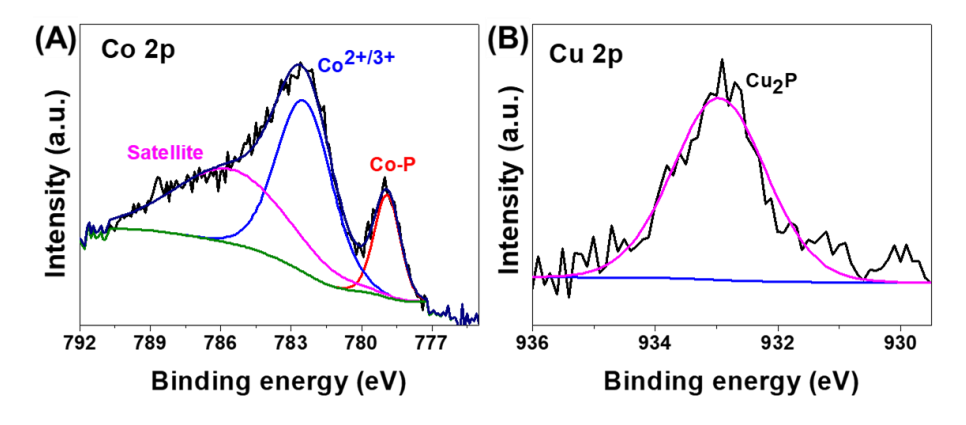


Figure S19. High resolution XPS spectra of (A) Co 2p and (B) Cu 2p of C-Co_{1.25}Cu_{0.75}P_x NRs, using 36.5 nm Co₂P seeds.

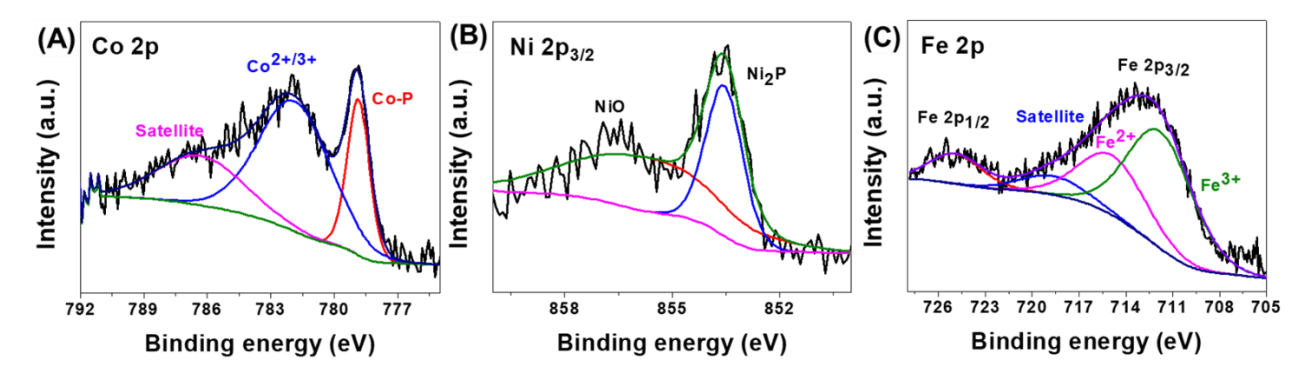


Figure S20. High resolution XPS spectra of **(A)** Co 2p, **(B)** Ni 2p and **(C)** Fe 2p of $Co_{1.01}Ni_{0.43}Fe_{0.56}P_x$ NRs, using 36.5 nm Co_2P seeds.

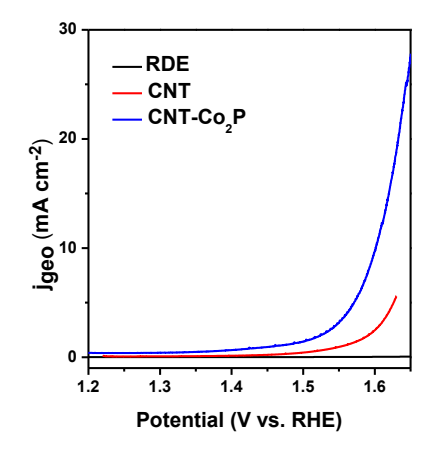


Figure S21. OER polarization curve of CNT-Co₂P NRs (36.5 nm), compared with blank glassy carbon rotating disk electrode (RDE) and blank CNTs, in 1.0 M KOH.

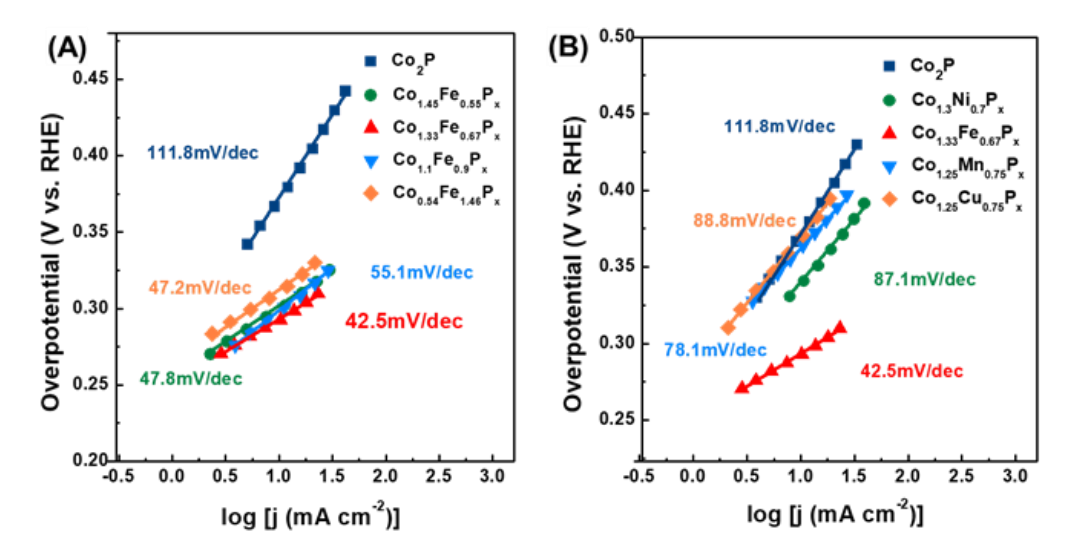


Figure S22. (A) Tafel slopes of C-Co₂P, -Co_{1.45}Fe_{0.55}P_x, -Co_{1.33}Fe_{0.67}P_x, -Co_{1.10}Fe_{0.90}P_x and -Co_{0.54}Fe_{1.46}P_x NRs catalysts. (B) Tafel slopes of C-Co₂P, -Co_{1.30}Ni_{0.70}P_x, -Co_{1.33}Fe_{0.67}P_x, -Co_{1.25}Mn_{0.75}P_x and -Co_{1.25}Cu_{0.75}P_x NRs catalysts. Syntheses were carried out using 36.5 nm Co₂P seeds, in 1.0 M KOH.

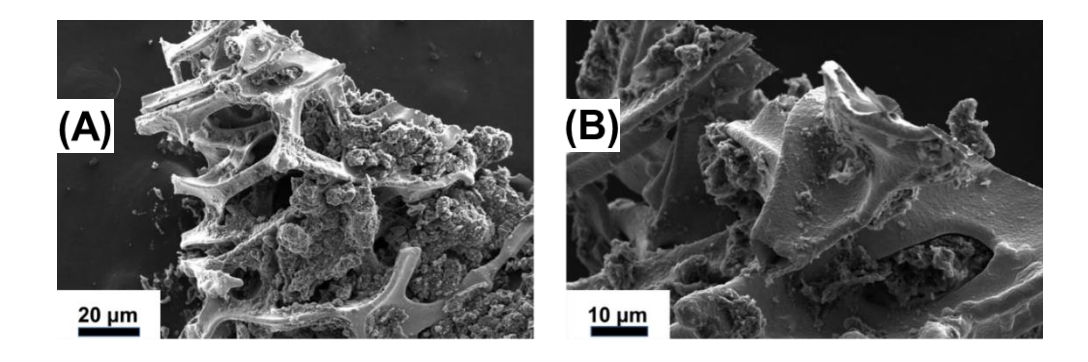


Figure S23. SEM images of CNT-Co_{1.33}Fe_{0.67}P_x NRs modified nickel foam, at different magnifications.

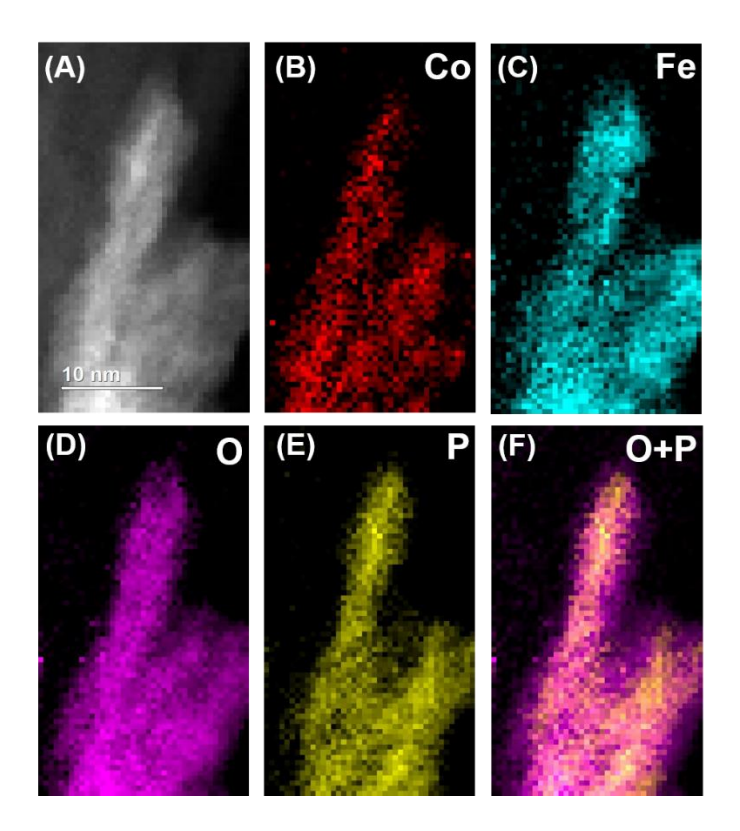


Figure S24. (A) STEM-HAADF image and (B-F) EELS 2-D elemental mappings of CNT-Co_{1.33}Fe_{0.67}P $_{\rm x}$ NRs after the stability test.